J. Fluid Mech. (2014), *vol.* 747, *pp.* 247–287. © Cambridge University Press 2014
doi:10.1017/jfm.2014.138

Investigation of Boussinesq dynamics using intermediate models based on wave–vortical interactions

Gerardo Hernandez-Duenas[1,†], Leslie M. Smith[1,2] and Samuel N. Stechmann[1,3]

[1]Department of Mathematics, University of Wisconsin–Madison, Madison, WI 53706, USA

[2]Department of Engineering Physics, University of Wisconsin–Madison, Madison, WI 53706, USA

[3]Department of Atmospheric and Oceanic Sciences, University of Wisconsin–Madison, Madison, WI 53706, USA

(Received 25 June 2013; revised 9 December 2013; accepted 8 March 2014; first published online 15 April 2014)

Nonlinear coupling among wave modes and vortical modes is investigated with the following question in mind: can we distinguish the wave–vortical interactions largely responsible for formation versus evolution of coherent, balanced structures? The two main case studies use initial conditions that project only onto the vortical-mode flow component of the rotating Boussinesq equations: (i) an initially balanced dipole and (ii) random initial data in the vortical modes. Both case studies compare quasi-geostrophic (QG) dynamics (involving only nonlinear interactions between vortical modes) to the dynamics of intermediate models allowing for two-way feedback between wave modes and vortical modes. For an initially balanced dipole with symmetry across the $\hat{\boldsymbol{x}}$-axis, the QG dipole will propagate along the $\hat{\boldsymbol{x}}$-axis while the trajectory of the Boussinesq dipole exhibits a cyclonic drift. Compared to a forced linear (FL) model with one-way forcing of wave modes by the vortical modes, the simplest intermediate model with two-way feedback involving vortical–vortical–wave interactions is able to capture the speed and trajectory of the dipole for roughly ten times longer at Rossby Ro and Froude Fr numbers $Ro = Fr \approx 0.1$. Despite its success at tracking the dipole, the latter intermediate model does not accurately capture the details of the flow structure within the adjusted dipole. For decay from random initial conditions in the vortical modes, the full Boussinesq equations generate vortices that are smaller than QG vortices, indicating that wave–vortical interactions are fundamental for creating the correct balanced state. The intermediate model with QG and vortical–vortical–wave interactions actually prevents the formation of vortices. Taken together these case studies suggest that: vortical–vortical–wave interactions create waves and thereby influence the evolution of balanced structures; vortical–wave–wave interactions take energy out of the wave modes and contribute in an essential way to the formation of coherent balanced structures.

Key words: rotating flows, stratified flows, wave–turbulence interactions

† Email address for correspondence: hernandez@math.wisc.edu

https://doi.org/10.1017/jfm.2014.138 Published online by Cambridge University Press

1. Introduction

The waves generated by frame rotation are called inertial waves (Greenspan 1968), and the waves caused by stable density/temperature stratification are referred to as internal gravity waves (e.g. Gill 1982). When rotation and stable stratification are present together, as in atmospheric and oceanic flows, the so-called inertia–gravity waves play an important role in transporting energy and momentum, in modulating weather, and in influencing mean circulations (Fritts & Alexander 2003; Wunsch & Ferrari 2004). Sources of wave activity in the middle atmosphere include topography, convection and wind shear (Fritts & Alexander 2003), and in the oceans these waves are excited by surface winds, tides and topography (Wunsch & Ferrari 2004). In addition, it is now understood that inertia–gravity waves can be spontaneously generated from balanced flows (Lorenz & Krishnamurthy 1987; O'Sullivan & Dunkerton 1995; Ford, McIntyre & Norton 2000; Plougonven & Zeitlin 2002; Vanneste & Yavneh 2004; Snyder *et al.* 2007; Zeitlin 2008; Vanneste 2013). Spatial resolutions of global models are currently too coarse to resolve all of the inertia–gravity waves (Fritts & Alexander 2003). Thus theoreticians and modellers continue to probe idealized models for information and insight into the many mechanisms for wave generation, as well as their influence on larger-scale balanced flows, with at least one important goal of refining parameterizations in global models (e.g. Ledwell *et al.* 2000; Warner & McIntyre 2001). The current study investigates the effects of waves on balanced flows, and in particular the role of nonlinear wave–vortical interactions in the formation and evolution of coherent balanced structures.

We consider the rotating Boussinesq equations valid for flows in which the depth of fluid motions is small compared to the density scale height (Spiegel & Veronis 1960; Vallis 2006). In the Boussinesq approximation, acoustic waves are filtered out and the statement of conservation of fluid mass reduces to the incompressibility constraint. In addition to the quadratic nonlinearity and pressure terms arising in fluid systems, frame rotation and buoyancy lead to linear terms in the statements of conservation of momentum and energy. The decomposition into vortical and wave components follows naturally from Fourier analysis of the (inviscid) linearized equations in an infinite or periodic domain. From here on we discuss periodic domains for which there are complementary numerical computations.

In the linear limit there exist two inertia–gravity waves and one vortical mode (named for its structure), which together form an orthogonal, divergence-free basis which can be used without loss of generality for representation of nonlinear solutions (see e.g. the book by Majda 2003). For each wavevector $\boldsymbol{k}$, the two inertia–gravity waves have oppositely signed wave frequencies $\sigma^{\pm}(\boldsymbol{k})$ given by the dispersion relation depending on rotation rate and buoyancy frequency; the vortical mode has zero frequency $\sigma^{0}(\boldsymbol{k}) = 0$. Thus the velocity $\boldsymbol{u}$ and density/temperature fluctuations θ may be expressed as

$$\begin{pmatrix} \boldsymbol{u} \\ \theta \end{pmatrix}(\boldsymbol{x}, t) = \sum_{\boldsymbol{k}} \sum_{s_{\boldsymbol{k}}=0,\pm} b^{s_{\boldsymbol{k}}}(\boldsymbol{k}, t)\boldsymbol{\phi}^{s_{\boldsymbol{k}}}(\boldsymbol{k}) \exp\left(\mathrm{i}\left(\boldsymbol{k}\cdot\boldsymbol{x} - \sigma^{s_{\boldsymbol{k}}}(\boldsymbol{k})t\right)\right), \tag{1.1}$$

where $\boldsymbol{\phi}^{s_{\boldsymbol{k}}}(\boldsymbol{k})$ is the eigenmode of type $s_{\boldsymbol{k}}$ ($s = \pm$ wave or $s = 0$ vortical) and $b^{s_{\boldsymbol{k}}}(\boldsymbol{k}, t)$ is an (unknown) amplitude. Using the decomposition (1.1), the equations for $\boldsymbol{u}$ and θ may be rewritten as evolution equations for the amplitudes $b^{s_{\boldsymbol{k}}}(\boldsymbol{k}, t)$:

https://doi.org/10.1017/jfm.2014.138 Published online by Cambridge University Press

$$\frac{\partial b^{s_k}(\boldsymbol{k},t)}{\partial t} = \sum_{\boldsymbol{k}+\boldsymbol{p}+\boldsymbol{q}=0} \sum_{s_p,s_q=0,\pm} C_{\boldsymbol{kpq}}^{s_k s_p s_q} \times \overline{b^{s_p}}(\boldsymbol{p},t)\overline{b^{s_k}}(\boldsymbol{q},t) \exp(\mathrm{i}(\sigma^{s_k}(\boldsymbol{k}) + \sigma^{s_p}(\boldsymbol{p}) + \sigma^{s_q}(\boldsymbol{q}))t), \tag{1.2}$$

where the overline denotes the complex conjugate. The quadratic nonlinearity in physical space appears as a convolution sum in Fourier space: each unknown mode amplitude $b^{s_k}(\boldsymbol{k},t)$ evolves by pair products of mode amplitudes $b^{s_p}(\boldsymbol{p},t)$ and $b^{s_q}(\boldsymbol{q},t)$, with a sum over wavevectors $\boldsymbol{p}$ and $\boldsymbol{q}$ where $\boldsymbol{k}+\boldsymbol{p}+\boldsymbol{q}=0$. Of course the mode amplitudes can be of any mode type $(\pm,0)$, and so (1.2) also involves a sum over mode types s_p, $s_q = \pm, 0$. The coupling coefficients $C_{\boldsymbol{kpq}}^{s_k s_p s_q}$ are computed from the known eigenmodes (for some explicit examples, see Remmel, Sukhatme & Smith 2013). Reflecting the dispersive nature of the inertia–gravity waves, the phase factor involving the triple sum of mode frequencies $\sigma^{s_k}(\boldsymbol{k}) + \sigma^{s_p}(\boldsymbol{p}) + \sigma^{s_q}(\boldsymbol{q})$ can be highly oscillatory in general, presenting a challenge for theoretical analyses and resolution of numerical computations.

Early analyses focused on resonant triad interactions for which the triple sum of mode frequencies is exactly zero (e.g. McComas & Bretherton 1977; Lelong & Riley 1991; Bartello 1995). In this case the phase factor in the convolution sum is unity and hence the problem of fast oscillations in the nonlinearity is removed. For large rotation rate and/or buoyancy frequency, one can show that exact resonances are the next-order correction to linear dynamics using perturbation analysis in an appropriately defined small parameter (e.g. Hasselmann 1962; Newell 1969). In terms of non-dimensional parameters, large rotation rate corresponds to small Rossby number Ro, defined as the ratio of the rotation time scale to a nonlinear time scale. Similarly, large buoyancy frequency corresponds to small Froude number Fr, defined as the ratio of the buoyancy time scale to a nonlinear time scale. Since vortical modes are zero-frequency modes, interactions between them are always exactly resonant. The celebrated quasi-geostrophic (QG) model first derived using scaling analysis (Charney 1948) may also be formally derived by allowing vortical modes to interact nonlinearly with themselves in the absence of waves (Salmon 1998; Smith & Waleffe 2002). The QG approximation is rigorously derived as the limiting dynamics for $Ro \sim Fr = \epsilon \to 0$ (Embid & Majda 1998; Babin, Mahalov & Nicolaenko 2000). QG theory is foundational for understanding the dynamics of large-scale atmospheric and oceanic flows, and is the basis for a vast literature (see the books by Gill 1982; Pedlosky 1982; Salmon 1998; Majda 2003; Vallis 2006). In addition to resonant interactions between vortical modes, there are also exact resonances involving wave modes. In particular, the theory of three-wave exact resonances is equivalent to weak turbulence (WT) theory (Zakharov, Lvov & Falkovich 1992), and has been used as a starting point to understand oceanic spectra (Hasselmann 1962; McComas & Bretherton 1977; Caillol & Zeitlin 2000; Lvov, Polzin & Tabak 2004).

While much insight has been gained by theory and computations of exact resonances, QG and WT both have limitations. For example, the vortical-mode resonances of QG dynamics cannot capture cyclone/anticyclone asymmetries observed in nature and in numerical computations (e.g. Polvani *et al.* 1994; Kuo & Polvani 2000; Muraki & Hakim 2001; Hakim, Snyder & Muraki 2002; Remmel & Smith 2009, hereafter referred to as RS09). Furthermore, as mentioned above, wave dynamics may play a crucial role in local and global budgets, for example, for enhanced vertical mixing over topography in the abyssal ocean (Ledwell *et al.* 2000; Wunsch & Ferrari 2004). As for deficiencies of WT theory, Waleffe (1993) showed that three-wave

https://doi.org/10.1017/jfm.2014.138 Published online by Cambridge University Press

exact resonances between inertial waves in purely rotating flows cannot transfer energy into the slow, two-dimensional wave modes corresponding to the large-scale, cyclonic vortical columns observed in physical and numerical experiments (Hopfinger, Browand & Gagne 1982; Smith & Waleffe 1999; see also Galtier 2003; Cambon, Rubinstein & Godeferd 2004). Similarly, three-wave exact resonances between gravity waves in strongly stratified flows cannot transfer energy into the slow wave modes corresponding to vertically sheared horizontal flows (Lelong & Riley 1991; Smith & Waleffe 2002). Using perturbative approaches, there are two separate bodies of literature exploring corrections to either QG theory or WT theory.

Adding near-resonant three-wave interactions is the natural perturbative step from WT theory, where near resonances have sum of mode frequencies small compared to the Rossby or Froude number (but not necessarily zero). In a perturbation expansion in powers of $\epsilon = Ro$ or $\epsilon = Fr$, linear dynamics is dominant at $O(1/\epsilon)$, exact resonances appear at $O(1)$ and near resonances become important at $O(\epsilon)$. In numerical computations, it has been shown that near-resonant three-wave interactions are responsible for generation of the slow wave modes corresponding to zonal flows on the β-plane, and cyclonic vortical columns in purely rotating flow (Smith & Lee 2005; Lee & Smith 2007). Near-resonant three-wave interactions have also been included in the WT theory of oceanic spectra (Lvov, Polzin & Yokoyama 2012). Reductions based on exact and near resonances have physical-space representation as integro-differential equations, for which numerical solution techniques have received less attention by fluid dynamicists compared to the widely used pseudo-spectral methods for partial differential equations (PDEs) (Boyd 2001; Canuto *et al.* 2006). In recent work, a PDE generalization of WT was derived, including exact, near- and non-resonant three-wave interactions (Remmel, Sukhatme & Smith 2010). A following study used pseudo-spectral numerical simulations to demonstrate that three-wave interactions are primarily responsible for the formation of vertically sheared horizontal flows in purely stratified turbulence (Remmel *et al.* 2013).

To correct QG, intermediate models of various types have been proposed and tested (e.g. McWilliams & Gent 1980; Allen 1993; Vallis 1996; Muraki, Snyder & Rotunno 1999; McIntyre & Norton 2000; Mohebalhojeh & Dritschel 2001). To eliminate secularities in perturbative intermediate models, it is necessary to introduce slaving principles whereby only the fast wave dynamics is expanded in powers of the Rossby number (Warn *et al.* 1995). Consequently such models are able to conserve potential vorticity (PV) as in the full dynamics, but slaving of waves to vortical-mode dynamics precludes the correct dispersion relation. The present work provides further testing of a different approach to modelling, based on wave–vortical interactions, first explored for the rotating shallow-water equations in RS09, and later for the three-dimensional (3D) Boussinesq equations (Remmel *et al.* 2010, 2013). The models are derived from projections of the full dynamical equations onto an entire class or classes of wave–vortical interactions. Some potentially interesting aspects of the approach are: (i) in general, it is non-perturbative in the sense that it relies on projections instead of expansions; (ii) an entire class or classes of wave–vortical interactions always correspond(s) to a system of PDEs for appropriate variables (see RS09 and appendix A); (iii) it has been used to correct both QG (exactly resonant, three-vortical-mode interactions) and WT (exactly resonant, three-wave interactions) and therefore in some sense provides a unifying framework to bridge the two.

Among the wave–vortical intermediate models is the PPG model, which adds vortical–vortical–wave interactions to the QG vortical–vortical–vortical interactions. (The acronym PPG was introduced in RS09 to as reference to PV–PV–gravity wave

https://doi.org/10.1017/jfm.2014.138 Published online by Cambridge University Press

interactions, here shortened to vortical–vortical–wave.) The Boussinesq PPG model is closely related to the first-order PV-inversion scheme of Muraki *et al.* (1999). While PPG does not slave waves to vortical modes and has the correct dispersion relation, the tradeoff is the non-conservation of PV. However, since both approaches include the effects of vortical–vortical–wave interactions beyond QG, the results we present here regarding the Boussinesq version of the PPG model are possibly relevant to some low-order PV-inversion methods as well. The next level of complexity within the wave–vortical model hierarchy is denoted P2G, so named because it adds vortical–wave–wave interactions to the PPG model. The P2G model can be viewed as a long-time extension of a forced linear (FL) model. FL models are restricted to short times since they only include one-way feedback between a balanced flow component and waves, while the P2G model incorporates full two-way feedback.

Some points to keep in mind while reading the rest of the paper are the following. PPG and P2G are projective variations of, respectively, a first-order PV-inversion scheme and a FL model based on expansions, and they provide an alternative conceptual framework for exploring non-QG behaviour. Except in the case of QG, the wave–vortical model hierarchy based on projections does not provide computational efficiency compared to the full Boussinesq equations. The wave–vortical decomposition associates the balanced flow component with projection onto the vortical eigenmodes, and the unbalanced flow component with a projection onto the wave eigenmodes. Thus, except in post-processing the numerical data, the wave–vortical decomposition always attributes vertical motions to the unbalanced flow component, unlike perturbative methods such as PV-inversion, which incorporate ageostrophic corrections into the definition of the balanced flow component.

Our numerical calculations focus on moderate values of the Rossby and Froude numbers $0.05 \leqslant Ro, Fr \leqslant 1$. We compare the wave–vortical intermediate model simulations to companion simulations of QG (when sensible), and to simulations of the full rotating Boussinesq dynamics. In the first part of the paper, we investigate the Boussinesq analogy of an initial value problem that has been studied using a perturbative approach, namely the evolution of a balanced dipole (Snyder *et al.* 2007; Viúdez 2007; Snyder, Plougonven & Muraki 2009; Wang, Zhang & Snyder 2009; Wang & Zhang 2010). Compared to the QG dynamics, the Boussinesq dynamics exhibit a cyclonic drift in the trajectory of the dipole, and we investigate how long the various models are able to track the dipole, and which classes of wave–vortical interactions are necessary to capture the detailed structure of the adjusted ageostrophic dipole. Our study is also closely related to Ribstein, Gula & Zeitlin (2010) who considered adjustment toward quasi-stationary coherent ageostrophic dipoles in rotating shallow-water flow (see also Kizner *et al.* 2008). In a second set of simulations, we investigate coherent structure formation starting from random initial conditions. Our goal is to provide a framework for understanding wave–vortical interactions, complementary to the understanding provided by asymptotic approaches for $Ro \to 0$ and/or $Fr \to 0$ (e.g. Plougonven & Zeitlin 2002; Zeitlin 2008; Snyder *et al.* 2009; Vanneste 2013). A main contribution is the ability to distinguish the roles of vortical–vortical–wave and vortical–wave–wave interactions beyond what can be concluded based on resonances (McComas & Bretherton 1977; Lelong & Riley 1991; Bartello 1995). We show that vortical–vortical–wave interactions create waves and thereby influence the evolution of balanced structures, but have a relatively small role in the generation of new coherent structures. By contrast, the vortical–wave–wave interactions take energy out of the wave modes and contribute in an essential way to structure formation and the establishment of the correct balanced state.

https://doi.org/10.1017/jfm.2014.138 Published online by Cambridge University Press

The remainder of the paper is organized as follows. Section 2 reviews the eigenmode decomposition of the rotating Boussinesq equations. Section 3 introduces the intermediate models using projection operators in physical space; the PPG model consisting of vortical–vortical–vortical and vortical–vortical–wave interactions is described in detail. In § 4, we consider the evolution of a balanced dipole and compare the results of the intermediate models to the full Boussinesq dynamics as well as to QG and to an FL model. Section 5 investigates decay from random initial conditions: most cases use initial conditions that project only onto the vortical modes, but to investigate robustness, we also consider one case of initial conditions that project only onto the wave modes. Also, for robustness of conclusions on the decay from random initial data in the vortical modes, we test the parameters $Ro \approx Fr \approx 0.2$, $Ro \approx 0.1$, $Fr \approx 1$ and $Ro \approx 1$, $Fr \approx 0.1$. A summary is given in § 6. Appendix A provides the re-formulation of the PPG model in terms of the streamfunction, potential and geostrophic imbalance. Appendix B completes the model hierarchy in terms of projectors.

2. The rotating Boussinesq equations

The main goal of the present work is to assess the importance of vortical–vortical–wave and vortical–wave–wave interactions for propagation and formation of coherent structures in three-dimensional rotating stratified flows at moderate Rossby and Froude numbers. Here we review the linear theory and eigenmode decomposition of the rotating Boussinesq equations in a periodic domain, which are the basis for the numerical computations presented in later sections.

The (inviscid) Boussinesq equations for vertically stratified flows rotating about the vertical $\hat{\boldsymbol{z}}$-axis in dimensional form are given by (see e.g. Majda 2003)

$$\left.\begin{aligned} &\frac{\mathrm{D}\boldsymbol{u}}{\mathrm{D}t} + f\hat{\boldsymbol{z}} \times \boldsymbol{u} + N\theta\hat{\boldsymbol{z}} = -\boldsymbol{\nabla} p, \\ &\frac{\mathrm{D}\theta}{\mathrm{D}t} - N\boldsymbol{u} \cdot \hat{\boldsymbol{z}} = 0, \\ &\boldsymbol{\nabla} \cdot \boldsymbol{u} = 0, \end{aligned}\right\} \tag{2.1}$$

where $\boldsymbol{u}$ is the velocity, $\mathrm{D}/\mathrm{D}t = \partial/\partial t + \boldsymbol{u} \cdot \boldsymbol{\nabla}$ is the material derivative, p is the effective pressure, and the density $\rho = \rho_0 + \bar{\rho}(z) + \rho'$ has been decomposed into a background $\rho_0 + \bar{\rho}(z)$ and fluctuating part ρ'. The Boussinesq approximation assumes that $|\rho'|, |\bar{\rho}(z)| \ll \rho_0$, valid for flows in which the depth of fluid motions is small compared to the density scale height (Spiegel & Veronis 1960; Vallis 2006). For linear background $\bar{\rho}(z) = -\alpha z$ with α a positive constant (for uniform stable stratification), the buoyancy frequency is $N = (g\alpha/\rho_0)^{1/2}$, where g is the gravitational constant. The Coriolis parameter $f = 2\Omega$ is twice the frame rotation rate Ω. The variable $\theta = (\alpha\rho_0/g)^{-1/2}\rho'$ is a simply the density fluctuation rescaled to have dimensions of velocity for convenience when manipulating equations and forming energies.

In a $2\pi \times 2\pi \times 2\pi$ periodic domain and in the linear limit, there are plane-wave solutions of the form

$$\begin{pmatrix} \boldsymbol{u} \\ \theta \end{pmatrix}(\boldsymbol{x}, t; \boldsymbol{k}) = \boldsymbol{\phi}(\boldsymbol{k}) \mathrm{e}^{\mathrm{i}(\boldsymbol{k}\cdot\boldsymbol{x} - \sigma(\boldsymbol{k})t)}, \tag{2.2}$$

where $\boldsymbol{\phi}(\boldsymbol{k}) = (\hat{\boldsymbol{u}}(\boldsymbol{k}), \hat{\theta}(\boldsymbol{k}))$ is the Fourier vector coefficient associated with the wavevector $\boldsymbol{k}$. There are only three modes per wavevector because of the

https://doi.org/10.1017/jfm.2014.138 Published online by Cambridge University Press

incompressibility constraint: two of these eigenmodes $\boldsymbol{\phi}^{\pm}(\boldsymbol{k})$ have non-zero frequency $\sigma^{\pm}(\boldsymbol{k})$ and the third one $\boldsymbol{\phi}^{0}(\boldsymbol{k})$ has zero frequency $\sigma^{0}(\boldsymbol{k}) = 0$. The latter is usually called a vortical mode, while the former are inertia–gravity waves. The dispersion relation for the inertia–gravity waves is

$$\sigma^{\pm}(\boldsymbol{k}) = \pm \frac{(N^2 k_h^2 + f^2 k_z^2)^{1/2}}{k}, \tag{2.3}$$

where $k = |\boldsymbol{k}|$, $k_h = (k_x^2 + k_y^2)^{1/2}$. The eigenfunctions for $\boldsymbol{k} \neq 0$ are given by

$$\boldsymbol{\phi}^{+} = \begin{cases} \dfrac{1}{\sqrt{2}\sigma k} \begin{pmatrix} \dfrac{k_z}{k_h}(\sigma k_x + \mathrm{i} k_y f) \\ \dfrac{k_z}{k_h}(\sigma k_y - \mathrm{i} k_x f) \\ -\sigma k_h \\ -\mathrm{i} N k_h \end{pmatrix} & \text{if } k_h \neq 0 \\ \begin{pmatrix} \dfrac{1+\mathrm{i}}{2} \\ \dfrac{1-\mathrm{i}}{2} \\ 0 \\ 0 \end{pmatrix} & \text{if } k_h = 0, \end{cases} \tag{2.4}$$

$\boldsymbol{\phi}^{-} = \overline{\boldsymbol{\phi}^{+}}$, and

$$\boldsymbol{\phi}^{0} = \frac{1}{\sigma k} \begin{pmatrix} N k_y \\ -N k_x \\ 0 \\ f k_z \end{pmatrix}, \tag{2.5}$$

where $\sigma = |\sigma^{\pm}(\boldsymbol{k})|$. In triply periodic domains, there are no mean flows and thus one may set the eigenmodes to zero for $\boldsymbol{k} = \boldsymbol{0}$. One can appreciate the importance of the the vortical modes (2.5) by considering conservation of PV $\mathrm{D}q/\mathrm{D}t = 0$, where $q = -(1/N)(f\hat{\boldsymbol{z}} + \boldsymbol{\nabla} \times \boldsymbol{u}) \cdot \boldsymbol{\nabla}(-Nz + \theta)$ (Gill 1982; Pedlosky 1982; Salmon 1998; Majda 2003; Vallis 2006). The wave modes (2.4) have zero linear PV and thus the conservation law is non-trivially satisfied by a projection onto the vortical modes with $q_{QG} = -(f/N)\partial\theta/\partial z + \hat{\boldsymbol{z}} \cdot (\boldsymbol{\nabla} \times \boldsymbol{u})$, which is the (non-constant) linear part of the total (quadratic) PV, also called the pseudo-PV. The 3D QG approximation to the Boussinesq system (2.1) satisfies conservation of pseudo-PV (Charney 1948) and can be formally derived by allowing the vortical modes to interact nonlinearly in the absence of wave modes (Salmon 1998; Smith & Waleffe 2002).

The eigenmodes $\boldsymbol{\phi}^{s_k}(\boldsymbol{k})$, $s_k = 0, \pm$, form an orthonormal basis for the space of divergence-free fields. Decomposing

$$\begin{pmatrix} \boldsymbol{u} \\ \theta \end{pmatrix}(\boldsymbol{x}, t) = \sum_{\boldsymbol{k}} \sum_{s_k = 0, \pm} b^{s_k}(\boldsymbol{k}, t) \boldsymbol{\phi}^{s_k}(\boldsymbol{k}) \exp\left(\mathrm{i}\left(\boldsymbol{k} \cdot \boldsymbol{x} - \sigma^{s_k}(\boldsymbol{k}) t\right)\right), \tag{2.6}$$

and using orthogonality leads to the equations

$$\frac{\partial b^{s_k}(\boldsymbol{k}, t)}{\partial t} = -\overline{\boldsymbol{\phi}^{s_k}}(\boldsymbol{k}) \cdot \begin{pmatrix} \widehat{\boldsymbol{u} \cdot \boldsymbol{\nabla} \boldsymbol{u}} \\ \widehat{\boldsymbol{u} \cdot \boldsymbol{\nabla} \theta} \end{pmatrix} \exp\left(\mathrm{i} \sigma^{s_k}(\boldsymbol{k}) t\right) \tag{2.7}$$

https://doi.org/10.1017/jfm.2014.138 Published online by Cambridge University Press

Model	Interactions allowed
QG	Vortical–vortical–vortical
PPG	Vortical–vortical–vortical $\oplus$ vortical–vortical–wave
P2G	Vortical–vortical–vortical $\oplus$ vortical–vortical–wave $\oplus$ vortical–wave–wave
Boussinesq (FB)	All

TABLE 1. Interactions allowed in the main model hierarchy.

for each wavevector $\boldsymbol{k}$ and for each class of eigenmodes $s_k = 0, \pm$. Equations (2.7) are equivalently written as

$$\frac{\partial b^{s_k}(\boldsymbol{k}, t)}{\partial t} = \sum_{\boldsymbol{k}+\boldsymbol{p}+\boldsymbol{q}=0} \sum_{s_p, s_q = 0, \pm} C_{\boldsymbol{kpq}}^{s_k s_p s_q} \times \overline{b^{s_p}}(\boldsymbol{p}, t)\ \overline{b^{s_k}}(\boldsymbol{q}, t) \exp(\mathrm{i}(\sigma^{s_k}(\boldsymbol{k}) + \sigma^{s_p}(\boldsymbol{p}) + \sigma^{s_q}(\boldsymbol{q}))t), \tag{2.8}$$

where $C_{\boldsymbol{kpq}}^{s_k s_p s_q}$ are the interaction coefficients (see Remmel *et al.* 2013). The reduced models studied here result from a restriction of the sum in (2.8) to selected classes of interactions $(s_k s_p s_q)$; in physical space this corresponds to a projection onto the selected wave–vortical interactions. This type of intermediate model was introduced in RS09 for the rotating shallow-water equations. Each such model automatically satisfies global energy conservation because each triad separately satisfies (Kraichnan 1973)

$$C_{\boldsymbol{kpq}}^{s_k s_p s_q} + C_{\boldsymbol{qkp}}^{s_q s_k s_p} + C_{\boldsymbol{pqk}}^{s_p s_q s_k} = 0. \tag{2.9}$$

As mentioned above, the 3D QG approximation is equivalent to keeping (000) interactions only and neglecting wave modes altogether. It was shown that the PPG model including (000), (00±) interactions (and all permutations; see § 3 and table 1 for the present work) gives close quantitative agreement with the full dynamics for decay from random, unbalanced initial conditions. The PPG model can be considered as the simplest model with two-way feedback between vortical modes and wave modes, and is closely related to the PV-inversion model considered in Muraki *et al.* (1999).

3. Reduced models

In this section, we describe the Boussinesq models analogous to those derived in RS09 for the shallow-water equations, and first derived for the rotating Boussinesq equations in Remmel's thesis (Remmel 2010). Here the model hierarchy is presented in physical space using projection operators. In such a decomposition, each model may be written as two separate vortical and wave-like subsystems communicating through the nonlinear interactions.

At the bottom of the hierarchy is the QG model retaining only the vortical-mode interactions, namely $(s_k s_p s_q) = (000)$. The vortical mode is updated by allowing only vortical-mode interactions in the nonlinear term on the right-hand-side of (2.8). This leads to a single physical-space PDE for the pseudo-PV (Smith & Waleffe 2002). In addition to allowing vortical–vortical–vortical (000) triad interactions, the PPG model also allows for vortical–vortical–wave (00±) interactions (and all permutations). In PPG, $b^0(\boldsymbol{k}, t)$ is updated by allowing vortical–vortical and vortical–wave interactions

https://doi.org/10.1017/jfm.2014.138 Published online by Cambridge University Press

on the right-hand-side of (2.8), and $b^{\pm}(\boldsymbol{k}, t)$ is updated by allowing vortical–vortical interactions on the right-hand-side of (2.8). One may consider PPG as the simplest model with two-way feedback between vortical modes and waves in the hierarchy.

In order to explicitly define PPG and the other models, we need to decompose the solution vector into its vortical and wave components. Let us define the vortical projector $(\cdot)^0$ as (see appendix A):

$$\begin{pmatrix} u \\ v \\ w \\ \theta \end{pmatrix}^0 = \begin{pmatrix} -\partial_y \\ \partial_x \\ 0 \\ -\dfrac{f}{N}\partial_z \end{pmatrix} \left(\nabla_h^2 + \frac{f^2}{N^2}\partial_z^2\right)^{-1} \left(\partial_x v - \partial_y u - \frac{f}{N}\partial_z \theta\right). \tag{3.1}$$

This operator projects a vector field onto the vortical modes $\sum_{\boldsymbol{k}} b^0(\boldsymbol{k},t)\boldsymbol{\phi}^0(\boldsymbol{k})\exp(\mathrm{i}\boldsymbol{k}\cdot\boldsymbol{x})$. The wave projector is defined as

$$(\cdot)^{\pm} = (\cdot) - (\cdot)^0, \tag{3.2}$$

so that the vector solution is decomposed into the vortical and wave components as

$$\begin{pmatrix} \boldsymbol{u} \\ \theta \end{pmatrix} = \begin{pmatrix} \boldsymbol{u} \\ \theta \end{pmatrix}^0 + \begin{pmatrix} \boldsymbol{u} \\ \theta \end{pmatrix}^{\pm}. \tag{3.3}$$

We now apply both projectors (3.1) and (3.2) to the Boussinesq equations (2.1). The decomposition (3.3) is applied both to the vector solution and to the nonlinear products $\boldsymbol{u}\cdot\nabla[\boldsymbol{u},\theta]^T$, yielding two coupled systems of equations:

$$\left.\begin{aligned} &\frac{\partial}{\partial t}\begin{pmatrix} \boldsymbol{u}^0 \\ \theta^0 \end{pmatrix} + \begin{pmatrix} \boldsymbol{u}^0\cdot\nabla\boldsymbol{u}^0 + \boldsymbol{u}^{\boldsymbol{0}}\cdot\nabla\boldsymbol{u}^{\pm} + \boldsymbol{u}^{\pm}\cdot\nabla\boldsymbol{u}^0 + \boldsymbol{u}^{\pm}\cdot\nabla\boldsymbol{u}^{\pm} \\ \boldsymbol{u}^0\cdot\nabla\theta^0 + \boldsymbol{u}^{\boldsymbol{0}}\cdot\nabla\theta^{\pm} + \boldsymbol{u}^{\pm}\cdot\nabla\theta^0 + \boldsymbol{u}^{\pm}\cdot\nabla\theta^{\pm} \end{pmatrix}^0 \\ &\qquad + \begin{pmatrix} f\hat{\boldsymbol{z}}\times\boldsymbol{u}^0 + N\theta^0\hat{\boldsymbol{z}} \\ -N\boldsymbol{u}^0\cdot\hat{\boldsymbol{z}} \end{pmatrix} = \begin{pmatrix} -\nabla p^0 \\ 0 \end{pmatrix}, \\ &\nabla\cdot\boldsymbol{u}^0 = 0, \end{aligned}\right\} \tag{3.4}$$

and

$$\left.\begin{aligned} &\frac{\partial}{\partial t}\begin{pmatrix} \boldsymbol{u}^{\pm} \\ \theta^{\pm} \end{pmatrix} + \begin{pmatrix} \boldsymbol{u}^0\cdot\nabla\boldsymbol{u}^0 + \boldsymbol{u}^{\boldsymbol{0}}\cdot\nabla\boldsymbol{u}^{\pm} + \boldsymbol{u}^{\pm}\cdot\nabla\boldsymbol{u}^0 + \boldsymbol{u}^{\pm}\cdot\nabla\boldsymbol{u}^{\pm} \\ \boldsymbol{u}^0\cdot\nabla\theta^0 + \boldsymbol{u}^{\boldsymbol{0}}\cdot\nabla\theta^{\pm} + \boldsymbol{u}^{\pm}\cdot\nabla\theta^0 + \boldsymbol{u}^{\pm}\cdot\nabla\theta^{\pm} \end{pmatrix}^{\pm} \\ &\qquad + \begin{pmatrix} f\hat{\boldsymbol{z}}\times\boldsymbol{u}^{\pm} + N\theta^{\pm}\hat{\boldsymbol{z}} \\ -N\boldsymbol{u}^{\pm}\cdot\hat{\boldsymbol{z}} \end{pmatrix} = \begin{pmatrix} -\nabla p^{\pm} \\ 0 \end{pmatrix}, \\ &\nabla\cdot\boldsymbol{u}^{\pm} = 0. \end{aligned}\right\} \tag{3.5}$$

This decomposition will be used in the next section to describe the models in physical space.

3.1. *Derivation of models using projectors in physical space*

In physical space, each model can be written as two separate systems, one accounting for the vortical component of the solution, and the other describing the evolution of the waves. This can be done by using the systems (3.4) and (3.5) and selecting only certain classes of nonlinear interactions. For instance, the vortical component in the

https://doi.org/10.1017/jfm.2014.138 Published online by Cambridge University Press

PPG model can only be influenced by vortical–vortical ($s_k s_p s_q = 000$) and vortical–wave nonlinear products ($s_k s_p s_q = 00\pm$) and ($s_k s_p s_q = 0 \pm 0$). The wave component on the other hand is evolved by vortical–vortical nonlinear products ($s_k s_p s_q = \pm 00$). As previously noted, the next-order model of Muraki *et al.* (1999) is closely related to a slaved version of the PPG model, and there is a similar relation between the PV-inversion model of McIntyre & Norton (2000) and the PPG model for the rotating shallow-water equations (RS09).

The subsystems satisfy constraints which reflect the fact that each one corresponds to either the vortical or wave component of the total system. Furthermore, the two systems are linked and communicate with each other through the nonlinear interactions, yielding a mode decomposition in physical space. For the PPG model, the two subsystems may be written as

$$\left.\begin{aligned} &\frac{\partial}{\partial t}\begin{pmatrix}\boldsymbol{u}^0\\ \theta^0\end{pmatrix} + \begin{pmatrix}\boldsymbol{u}^0\cdot\boldsymbol{\nabla}\boldsymbol{u}^0 + \boldsymbol{u}^{\boldsymbol{0}}\cdot\boldsymbol{\nabla}\boldsymbol{u}^{\pm} + \boldsymbol{u}^{\pm}\cdot\boldsymbol{\nabla}\boldsymbol{u}^0\\ \boldsymbol{u}^0\cdot\boldsymbol{\nabla}\theta^0 + \boldsymbol{u}^{\boldsymbol{0}}\cdot\boldsymbol{\nabla}\theta^{\pm} + \boldsymbol{u}^{\pm}\cdot\boldsymbol{\nabla}\theta^0\end{pmatrix}^0 \\ &\qquad\qquad + \begin{pmatrix}f\hat{\boldsymbol{z}}\times\boldsymbol{u}^0 + N\theta^0\hat{\boldsymbol{z}}\\ -N\boldsymbol{u}^0\cdot\hat{\boldsymbol{z}}\end{pmatrix} = \begin{pmatrix}-\boldsymbol{\nabla}p^0\\ 0\end{pmatrix},\\ &\boldsymbol{\nabla}\cdot\boldsymbol{u}^0 = 0,\\ &w^0 = 0,\\ &\theta^0 + \frac{f}{N}\frac{\partial\psi^0}{\partial z} = 0, \quad \nabla_h^2\psi^0 = v_x^0 - u_y^0,\\ &\overline{u^0}(z) = 0, \quad \overline{v^0}(z) = 0, \end{aligned}\right\} \tag{3.6}$$

where $\overline{(\cdot)}$ denotes the horizontal mean, and

$$\left.\begin{aligned} &\frac{\partial}{\partial t}\begin{pmatrix}\boldsymbol{u}^{\pm}\\ \theta^{\pm}\end{pmatrix} + \begin{pmatrix}\boldsymbol{u}^0\cdot\boldsymbol{\nabla}\boldsymbol{u}^0\\ \boldsymbol{u}^0\cdot\boldsymbol{\nabla}\theta^0\end{pmatrix}^{\pm} + \begin{pmatrix}f\hat{\boldsymbol{z}}\times\boldsymbol{u}^{\pm} + N\theta^{\pm}\hat{\boldsymbol{z}}\\ -N\boldsymbol{u}^{\pm}\cdot\hat{\boldsymbol{z}}\end{pmatrix} = \begin{pmatrix}-\boldsymbol{\nabla}p^{\pm}\\ 0\end{pmatrix},\\ &\boldsymbol{\nabla}\cdot\boldsymbol{u}^{\pm} = 0,\\ &\nabla_h^2\psi^{\pm} - \frac{f}{N}\frac{\partial\theta^{\pm}}{\partial z} = 0, \quad \nabla_h^2\psi^{\pm} = v_x^{\pm} - u_y^{\pm}. \end{aligned}\right\} \tag{3.7}$$

The additional constraints in the two subsystems above can be interpreted in terms of a streamfunction, potential and geostrophic imbalance (see appendix A for more details). In the first subsystem the condition $w^0 = 0$ together with continuity indicates that the solution has no velocity potential. The imbalance $\theta^0 + (f/N)\partial\psi^0/\partial z$ also vanishes and the horizontal mean of the horizontal velocity $\overline{\boldsymbol{u}_h}$ is zero. As a result, the solution to the first subsystem is given by a streamfunction. Furthermore, the vortical component of the pressure $p^0 = f\psi^0$ is balanced by the linear terms of the first subsystem such that

$$\begin{pmatrix}f\hat{\boldsymbol{z}}\times\boldsymbol{u}^0 + N\theta^0\hat{\boldsymbol{z}}\\ -N\boldsymbol{u}^0\cdot\hat{\boldsymbol{z}}\end{pmatrix} = \begin{pmatrix}-\boldsymbol{\nabla}p^0\\ 0\end{pmatrix}. \tag{3.8}$$

In the second subsystem, the linear PV $\nabla_h^2\psi^{\pm} - (f/N)\partial\theta^{\pm}/\partial z = 0$ vanishes, guaranteeing that this subsystem evolves the wave component of the total solution only.

https://doi.org/10.1017/jfm.2014.138 Published online by Cambridge University Press

The total model solution is obtained by adding the two subsystems. This allows us to write the PPG model in a more concise way:

$$\left.\begin{aligned} &\frac{\partial}{\partial t}\begin{pmatrix}\boldsymbol{u}\\ \theta\end{pmatrix}+\begin{pmatrix}\boldsymbol{u}^0\cdot\nabla\boldsymbol{u}^0+\boldsymbol{u}^{\boldsymbol{0}}\cdot\nabla\boldsymbol{u}^{\pm}+\boldsymbol{u}^{\pm}\cdot\nabla\boldsymbol{u}^0\\ \boldsymbol{u}^0\cdot\nabla\theta^0+\boldsymbol{u}^{\boldsymbol{0}}\cdot\nabla\theta^{\pm}+\boldsymbol{u}^{\pm}\cdot\nabla\theta^0\end{pmatrix}^0+\begin{pmatrix}\boldsymbol{u}^0\cdot\nabla\boldsymbol{u}^0\\ \boldsymbol{u}^0\cdot\nabla\theta^0\end{pmatrix}^{\pm}\\ &\qquad\qquad+\begin{pmatrix}f\hat{\boldsymbol{z}}\times\boldsymbol{u}+N\theta\hat{\boldsymbol{z}}\\ -N\boldsymbol{u}\cdot\hat{\boldsymbol{z}}\end{pmatrix}=\begin{pmatrix}-\nabla p\\ 0\end{pmatrix},\\ &\nabla\cdot\boldsymbol{u}=0.\end{aligned}\right\}\tag{3.9}$$

In (3.9), the projection of the nonlinear products select the desired interactions, and is equivalent to (2.8) keeping vortical–vortical–vortical and vortical–vortical–wave interactions only. For completeness, the description of the rest of the models is included in appendix B.

3.2. *A forced linear model*

A forced linear (FL) model may be derived by assuming that the solution can be decomposed as a balanced component plus a small variation, and then linearizing the advection terms about the balanced state (Snyder *et al.* 2009). By construction, such a model is expected to be accurate for relatively small Rossby and Froude numbers and relatively short times, starting from balanced initial conditions. For the dipole computations of § 4, we will compare an FL model to the model hierarchy described in table 1.

The FL model is obtained by splitting

$$\begin{pmatrix}\boldsymbol{u}\\ \theta\end{pmatrix}=\begin{pmatrix}\tilde{\boldsymbol{u}}\\ \tilde{\theta}\end{pmatrix}+\begin{pmatrix}\boldsymbol{u}'\\ \theta'\end{pmatrix},\tag{3.10}$$

where $[\tilde{\boldsymbol{u}},\tilde{\theta}]^T$ is the balanced component of the flow. The deviation $[\boldsymbol{u}',\theta']^T$ from the balanced solution is evolved according to a linearization of the nonlinear products about the balanced state:

$$\left.\begin{aligned} &\frac{\partial}{\partial t}\begin{pmatrix}\boldsymbol{u}'\\ \theta'\end{pmatrix}+\begin{pmatrix}\tilde{\boldsymbol{u}}\cdot\nabla\boldsymbol{u}'+\boldsymbol{u}'\cdot\nabla\tilde{\boldsymbol{u}}\\ \tilde{\boldsymbol{u}}\cdot\nabla\theta'+\boldsymbol{u}'\cdot\nabla\tilde{\theta}\end{pmatrix}+\begin{pmatrix}f\hat{\boldsymbol{z}}\times\boldsymbol{u}'+N\theta'\hat{\boldsymbol{z}}\\ -N\boldsymbol{u}'\cdot\hat{\boldsymbol{z}}\end{pmatrix}\\ &\qquad\qquad=\begin{pmatrix}-\nabla p'\\ 0\end{pmatrix}-\frac{\partial}{\partial t}\begin{pmatrix}\tilde{\boldsymbol{u}}\\ \tilde{\theta}\end{pmatrix}-\begin{pmatrix}\tilde{\boldsymbol{u}}\cdot\nabla\tilde{\boldsymbol{u}}\\ \tilde{\boldsymbol{u}}\cdot\nabla\tilde{\theta}\end{pmatrix},\\ &\nabla\cdot\boldsymbol{u}'=0.\end{aligned}\right\}\tag{3.11}$$

The part of the nonlinear term involving only the balanced flow component $[\tilde{\boldsymbol{u}},\tilde{\theta}]^T$ appears as a forcing term in the equations for the deviation $[\boldsymbol{u}',\theta']^T$, and hence the name 'forced linear model'. For simplicity, here we adopt the most basic version of the FL model where the balanced flow component $\widetilde{(\cdot)}$ is defined to be the solution to the QG equation (the projection onto the vortical modes). The latter simple version of (3.11) is sufficient for the illustration of § 4; however ageostrophic corrections can be included in the definition of balance $\widetilde{(\cdot)}$, as described in Snyder *et al.* (2009). Note that our simple FL model allows interactions of the type $(s_k s_p s_q = \pm 0 \pm)$, $(s_k s_p s_q = \pm \pm 0)$ and $(s_k s_p s_q = \pm 00)$ with one-way feedback onto the wave modes.

https://doi.org/10.1017/jfm.2014.138 Published online by Cambridge University Press

3.3. *Numerical scheme and parameter values*

The numerical computations use a standard 3D periodic pseudo-spectral method with 2/3 dealiasing rule, as described in Smith & Waleffe (2002). The time integration is a third-order Runge–Kutta scheme, and linear terms are treated with integrating factors. Hyperdiffusion/hyperviscosity damping of the form $\nu\nabla^{16}$ is used in all evolution equations with coefficient $\nu = 10^{-28}$ for the resolution considered of 192^3 Fourier modes. The time step is chosen as $\Delta t = \min\left(k_m^{-1}v_{max}^{-1}, 2\pi/(10N)\right)$, where $v_{max} = \max(\max_x u, \max_x v, \max_x w)$, and k_m is the highest available wavenumber allowed by dealiasing.

4. Evolution of a balanced dipole vortex

For a first test of the models described in § 3 and table 1, we consider the time evolution of an initially balanced flow consisting of a large-scale, coherent dipole. Balanced monopoles and dipoles have been used as idealized models of atmospheric jet streaks, which are localized regions of high-speed flow within a larger zonal jet stream (see e.g. Cunningham & Keyser 2004; Snyder *et al.* 2007, 2009, and references therein). We will be interested in how wave–vortical interactions influence the speed and trajectory of the dipole (§§ 4.1–4.3) and its structure (§ 4.3). Evolution of a surface QG dipole was investigated in Snyder *et al.* (2007, 2009). They showed that, after an initial adjustment period, the structure of the dipole is modified to include a quasi-stationary oscillation in the vertical velocity, moving at the speed of the dipole. Here we consider a similar initial condition based on the dipole given by Flierl (1987) and focus on the evolution and structure of the adjusted dipole.

The streamfunction ψ of the Flierl (1987) 3D QG dipole satisfies the equation

$$\left[\frac{\partial^2}{\partial x^2} + \frac{\partial^2}{\partial y^2} + \frac{f^2}{N^2}\frac{\partial^2}{\partial z^2}\right]\psi = \beta\ \delta(\boldsymbol{x} - \boldsymbol{x}_{\boldsymbol{0}}^{+}) - \beta\ \delta(\boldsymbol{x} - \boldsymbol{x}_{\boldsymbol{0}}^{-}), \tag{4.1}$$

where δ is the Dirac delta function and the dipole has vortices of strength $\pm\beta$ at the poles $\boldsymbol{x}_0^{\pm}$. For $\boldsymbol{x}_0^{\pm} = (\pi,\ \pi \pm a/2,\ \pi \pm h/2)$, QG dynamics will propagate the dipole along the $\hat{\boldsymbol{x}}$-direction at $x = \pi$ with theoretical speed

$$c = \frac{N\beta a}{4\pi f}\left(a^2 + \frac{N^2}{f^2}h^2\right)^{-3/2}. \tag{4.2}$$

For the numerical computations, we approximate the Dirac delta functions by Gaussian functions to smooth out singularities near the two poles. The initial streamfunction in the $2\pi \times 2\pi \times 2\pi$ periodic domain is given by

$$\psi = \left[\frac{\partial^2}{\partial x^2} + \frac{\partial^2}{\partial y^2} + \frac{f^2}{N^2}\frac{\partial^2}{\partial z^2}\right]^{-1} D(\boldsymbol{x}), \tag{4.3}$$

where

$$D(\boldsymbol{x}) := \frac{1}{(2\pi\gamma)^{3/2}}\left(\beta\ \exp\left(-\|\boldsymbol{x} - \boldsymbol{x}_0^{+}\|^2/2\gamma\right) - \beta\ \exp\left(-\|\boldsymbol{x} - \boldsymbol{x}_0^{-}\|^2/2\gamma\right)\right), \tag{4.4}$$

with γ constant. For our simulations, we choose the following dipole parameters: $a = 0.5$, $h = 0.5$, $\beta = 10$ and $\gamma = 1/128$. The Froude number $Fr = [U]/(N[L])$,

https://doi.org/10.1017/jfm.2014.138 Published online by Cambridge University Press

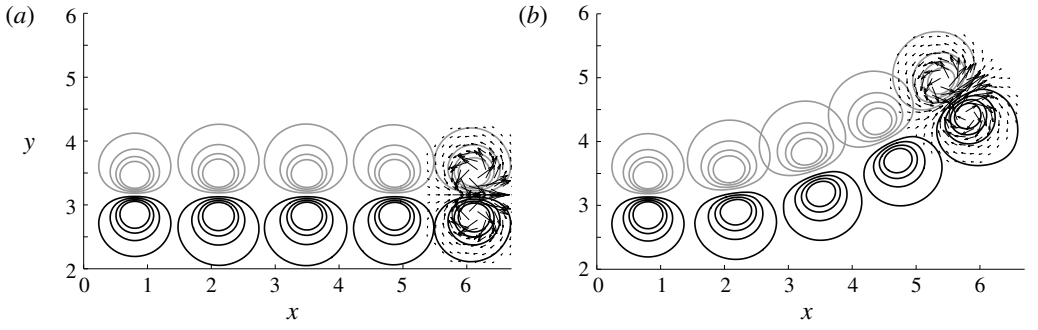


FIGURE 1. Contours of the streamfunction with values $\psi = \pm 0.25, \pm 0.5, \pm 0.75, \pm 1$ at $z = \pi$ and times $t = 0, 25, 50, 75, 100$ for (a) QG and (b) FB (full Boussinesq), for an initially balanced dipole with $Ro \approx Fr \approx 0.2$. The grey and black lines denote negative and positive values respectively. Arrows indicate the horizontal velocity vector field (u, v) near the dipole at $t = 100$ and $z = \pi$.

Rossby number $Ro = [U]/(f[L])$ and time scale $T_i = [L]/[U]$ are defined based on the maximum initial velocity $[U] = \max(\max_{\boldsymbol{x}} u, \max_{\boldsymbol{x}} v, \max_{\boldsymbol{x}} w)$ and characteristic length $[L] = 2a$. This initial time scale will be used to rescale the time as $t' = t/T_i$ (and the prime will be dropped). The values of the Coriolis parameter f and the buoyancy frequency N are decreased for the test cases in §§ 4.1–4.3, respectively, such that the Froude and Rossby numbers increase from $Ro = Fr = 0.05$ to 0.1 and 0.2.

Using the initial conditions in § 4.3 ($Ro = Fr = 0.2$, $T_i = 5.16 \times 10^{-2}$), figure 1 shows contours of the streamfunction with values $\psi = \pm 0.25, \pm 0.5, \pm 0.75, \pm 1$ at $z = \pi$ and times $t = 0, 25, 50, 75, 100$ for QG (a) and FB (b). The QG dipole moves steadily along a horizontal line at a roughly constant speed, which is approximately the theoretical speed $c = 1.13$ given by (4.2) (Flierl 1987). From figure 1(a), one can see that the distance between the first and last dipole is roughly $d = 5.8$, and can be computed as $d = c \times 100 \times T_i$ with $c = 1.13$ and $T_i = 5.16 \times 10^{-2}$. The horizontal velocity vectors $\boldsymbol{u}_h = (u, v)$ in the centre of the dipole show a 'jet streak'. In addition to a modified trajectory, the velocity and vorticity of the Boussinesq dipole reflect ageostrophic adjustment (§ 4.3). The formation of frontal wavepackets and the associated ageostrophic vorticity vector was studied by Viúdez (2007). FL models were investigated in Snyder *et al.* (2009), Wang *et al.* (2009), Wang & Zhang (2010) and Wang, Zhang & Epifanio (2010). In §§ 4.1 and 4.2, we compare streamfunction contours and trajectories of the QG, FL, PPG, P2G and FB systems for $Ro = Fr = 0.05$, 0.1, respectively. In § 4.3, we compare streamfunction contours, trajectories, vertical velocities and vertical vorticities of the PPG, P2G and FB systems for the larger value $Ro = Fr = 0.2$.

4.1. *Model comparison for* $Ro = Fr = 0.05$

In this section, the initial conditions consist of the dipole described above with characteristic scales $[U] = 22.85$, $T_i = 5.16 \times 10^{-2}$, and $[L] = 1.18$. The values of f and N are chosen so that the initial Froude and Rossby numbers are both $Fr = Ro = 0.05$. One may follow the dipole for each model in the frame of reference moving at the theoretical speed c of the QG dipole given by (4.2). Then at time $t = 50$ and vertical height $z = \pi$, figure 2(a,b,c) shows contours of the QG, FL and PPG model streamfunctions (thick lines) with values $\psi = \pm 0.25, \pm 0.5, \pm 0.75, \pm 1$, where the black

https://doi.org/10.1017/jfm.2014.138 Published online by Cambridge University Press

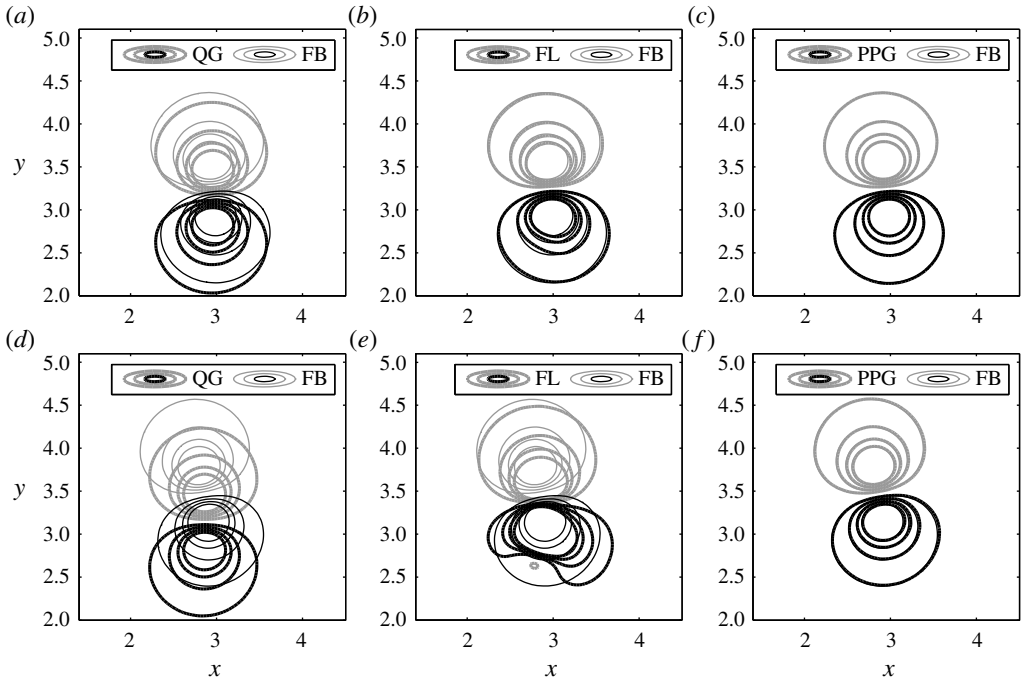


FIGURE 2. $Fr = Ro = 0.05$. Contours of the streamfunction with values $\psi = \pm 0.25$, ± 0.5, ± 0.75, ± 1 at $z = \pi$ and (*a*,*b*,*c*) $t = 50$; (*d*,*e*,*f*) $t = 80$. The grey and black lines denote negative and positive values, respectively. In all plots, thin lines correspond to FB contours, while thick lines are the contours corresponding to one of the models: (*a*,*d*) QG, (*b*,*e*) FL, (*c*,*f*) PPG. The position of the dipoles has been shifted to the centre of the domain.

and grey lines indicate positive and negative values, respectively. The corresponding FB dipole is included (thin lines) on top of each model dipole to visualize the agreement of each model with the full system. At this small $Ro = Fr = 0.05$, the QG and FB dipoles remain close (figure 2*a*,*d*) in a sense that will be quantified shortly. One expects even better agreement between FB and the models PPG and FL, at least for a short period time. Indeed, the differences at $t = 50$ are imperceptible to the eye (figure 2*b*,*c*). The P2G model is excluded from this plot, since it is even closer to FB than PPG.

Even for this relatively small $Ro = Fr = 0.05$, the FB dipole drifts away from the horizontal QG trajectory after a longer time. Figure 2(*d*) shows a more pronounced deviation of FB from QG at time $t = 80$. When the FB dipole deviates significantly from the balance state, the FL model assumptions are no longer valid. At time $t = 80$, one can see that the FL dipole begins to break down (figure 2*e*), while the PPG model maintains the dipole coherent structure of FB, and again differences are imperceptible to the eye.

In order to provide more quantitative information about the differences between the models and the FB dynamics, we measure the relative L^2 norm of the streamfunction error as a function of time, defined by

$$d_\psi(t) = \frac{\|\psi - \psi_{FB}\|_{L^2}}{\|\psi_{FB}\|_{L^2}}, \tag{4.5}$$

https://doi.org/10.1017/jfm.2014.138 Published online by Cambridge University Press

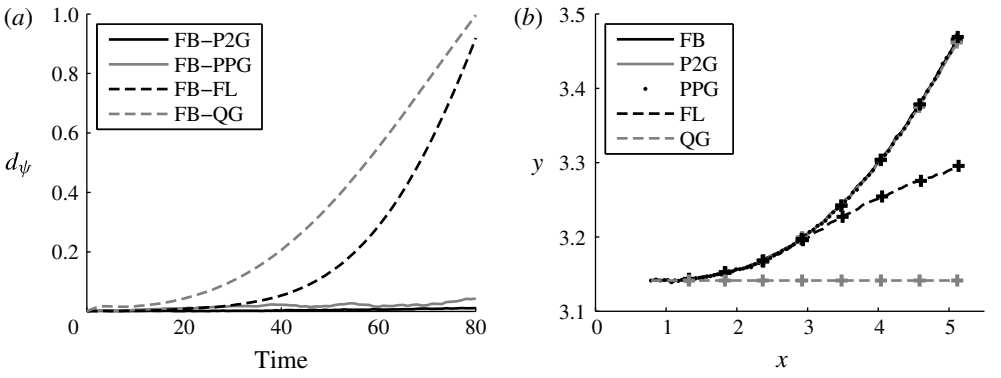


FIGURE 3. $Fr = Ro = 0.05$. (*a*) A measure of the relative error $d_\psi(t)$ between each model and the full system (see (4.5)). (*b*) The centre of the dipole/location of the jet $\boldsymbol{j}_\psi(t)$ (4.8) from 0 to 80 time units. At the initial time, the dipole location is shifted to the left boundary. A '+' symbol has been added every 10 time units.

where ψ denotes the streamfunction under consideration, and ψ_{FB} is the streamfunction of the FB model. In addition, the centre of each pole of the dipole in the horizontal plane at $z = \pi$ is approximated by a weighted average as

$$\boldsymbol{p}_\psi^\pm(t) = \frac{\displaystyle\int_{\Omega^\pm} (x, y)\, \psi(x, y, \pi)\, \mathrm{d}x\, \mathrm{d}y}{\displaystyle\int_{\Omega^\pm} \psi(x, y, \pi)\, \mathrm{d}x\, \mathrm{d}y} \in \mathbb{R}^2, \tag{4.6}$$

where $\Omega^\pm$ is the region contained in the horizontal plane $z = \pi$:

$$\Omega^\pm = \left\{ (x, y, \pi) \mid \pm\ \psi(x, y, \pi) \geqslant 0.5 \max_{z=\pi} \pm\psi > 0 \right\}. \tag{4.7}$$

The centre of the jet is defined as

$$\boldsymbol{j}_\psi(t) := (\boldsymbol{p}_\psi^+(t) + \boldsymbol{p}_\psi^-(t))/2. \tag{4.8}$$

Figure 3(*a*) shows $d_\psi(t)$ as a function of time for the different models, and provides a measure of how much each model deviates from the solution given by the Boussinesq system. During the first 30 time units, the FL, PPG and P2G models all show minimal relative error $d_\psi(t)$. For times up to $t = 80$, the FL model is more accurate than QG because it accounts for wave corrections via one-way feedback from vortical modes to waves. However, after 40 time units, FL begins to deviate significantly from FB, while PPG and P2G remain quantitatively accurate by this measure $d_\psi(t)$. Figure 3(*b*) shows the trajectory of the centre of the jet in each model as tracked by the function $\boldsymbol{j}_\psi(t)$. The PPG and P2G models give the best results and their jet-centres coincide with the FB jet-centre for times at least as large as $t = 80$. In §§ 4.2 and 4.3 we test the performance of the FL, PPG and P2G models using larger Froude and Rossby numbers.

https://doi.org/10.1017/jfm.2014.138 Published online by Cambridge University Press

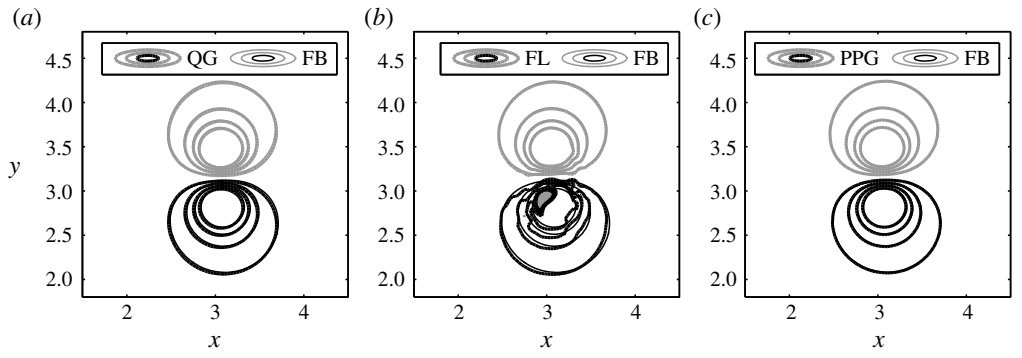


FIGURE 4. $Fr = Ro = 0.1$. Contours of the streamfunction with values $\psi = \pm 0.25, \pm 0.5, \pm 0.75, \pm 1$ at $z = \pi$, $t = 16$ for FB (thin lines) and the models (thick lines): (*a*) QG, (*b*) FL, and (*c*) PPG. The grey and black lines denote negative and positive values, respectively. The position of the dipoles has been shifted to the centre of the domain.

4.2. $Ro = Fr = 0.1$

Computations in this section use the same initial conditions as in § 4.1, but here we consider a smaller Coriolis parameter and buoyancy frequency so as to increase the initial Rossby and Froude numbers to $Ro = Fr = 0.1$. Larger values of Froude and Rossby numbers correspond to regimes farther from the QG dynamics. As a result, we expect the FL model for $Ro = Fr = 0.1$ to be valid for a shorter period of time than for the $Ro = Fr = 0.05$ case of the previous section.

As in figure 2, we follow the dipole for each model in the frame of reference moving at the theoretical speed c of the QG dipole given by (4.2). Comparing figures 2 and 4, the FL model is visibly different from FB at $t = 16$, $z = \pi$, $Ro = Fr = 0.1$, whereas the FL and FB dipoles are visibly the same at $t = 50$, $z = \pi$, $Ro = Fr = 0.05$. As expected, the FL model is valid for shorter times at larger $Ro = Fr$. Figure 5(*a*) shows that FL is quantitatively more accurate than QG for times $t < 10$, but actually has larger error than QG for approximately $t > 12$. As discussed and illustrated in Snyder (1999), growth of errors in the position/amplitude of finite-amplitude flow features occurs on the advective timescale of the base state, and in this case we observe error growth starting at $t \approx 11$ for the simplistic FL model (3.11) used here. Figure 4 exhibits good visual agreement between FB and all three of QG, PPG and P2G (not shown) at the relatively early time $t = 16$.

By time $t = 80$, a comparison between figures 2(*d*) and 6(*a*) shows that the FB dipole has drifted farther from the x-axis for $Ro = Fr = 0.1$ than in the case $Ro = Fr = 0.05$. For the larger $Ro = Fr = 0.1$, we observe that the dipole remains coherent in PPG and P2G up to times at least as large as $t = 100$, and its trajectory is quantitatively accurate for about ten times longer than FL (figure 5*a*,*c*). The relative error for PPG and P2G is less than 10 % for times up to approximately $t \approx 50$ (figure 5*b*), after which time it is clear that P2G provides a more faithful approximation to the FB dynamics.

4.3. $Ro = Fr = 0.2$

Repeating the QG, PPG, P2G and FB dipole computations for $Ro = Fr = 0.2$, figure 7 shows the pole-centre/jet trajectory for $0 \leqslant t \leqslant 100$. We do not run the FL model

https://doi.org/10.1017/jfm.2014.138 Published online by Cambridge University Press

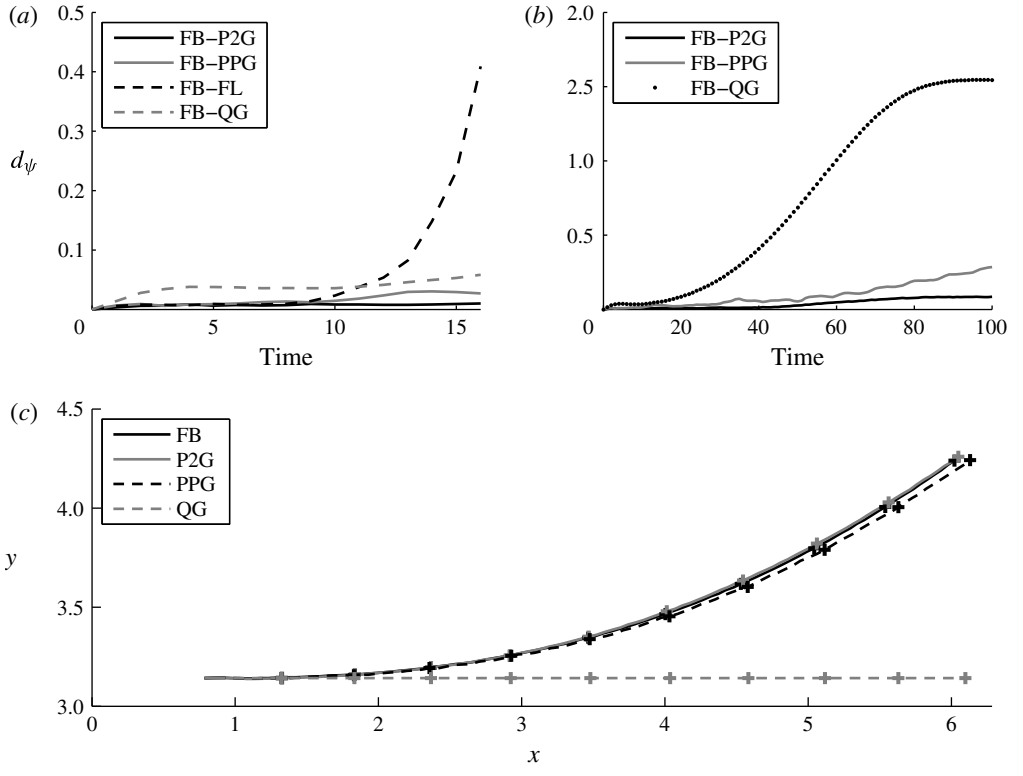


FIGURE 5. $Fr = Ro = 0.1$. (*a*,*b*) The relative error d_ψ is shown as a function of time for each model: (*a*) the deviations from FB of QG, FL, PPG, and P2G for $0 \leqslant t \leqslant 16$; (*b*) the deviations from FB of the wave–vortical models P2G and PPG, together with QG, for $0 \leqslant t \leqslant 100$. (*c*) The approximate position of the dipole centre/jet $\boldsymbol{j}_\psi$ in each model for $0 \leqslant t \leqslant 100$. At the initial time, the dipole location is shifted to the left boundary. A '+' symbol has been added every 10 time units.

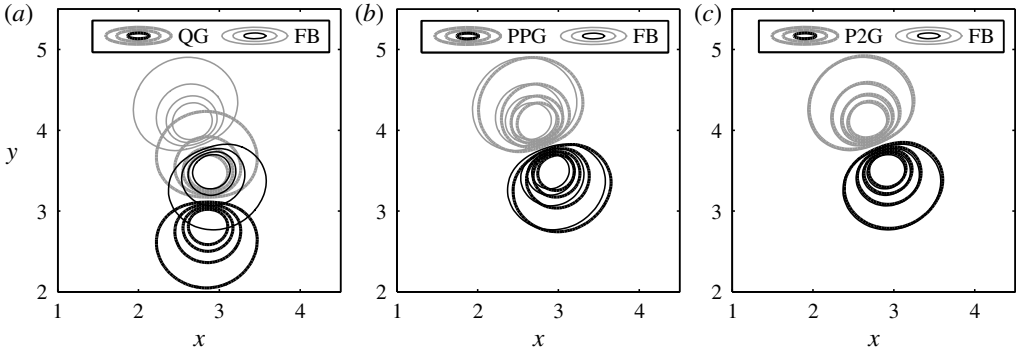


FIGURE 6. $Fr = Ro = 0.1$. Contours of the streamfunction with values $\psi = \pm 0.25$, ± 0.5, ± 0.75, ± 1 at $z = \pi$, $t = 80$ for FB (thin lines) and for (thick lines): (*a*) QG, (*b*) PPG and (*c*) P2G. The grey and black lines denote negative and positive values respectively. The position of the dipoles has been shifted to the centre of the domain.

https://doi.org/10.1017/jfm.2014.138 Published online by Cambridge University Press

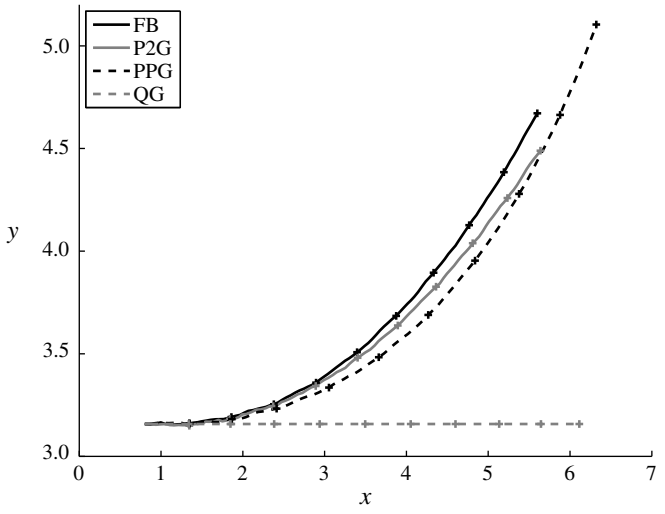


FIGURE 7. $Fr = Ro = 0.2$. Approximate location of the dipole centre/jet $\boldsymbol{j}_\psi$ for each model for $0 \leqslant t \leqslant 100$. At the initial time, the dipole is shifted to the left boundary. A '+' symbol has been added every 10 time units.

for this case since the FL model did not perform well for $t > 10$ at $Ro = Fr = 0.1$, and is expected to be valid for even shorter times when $Ro = Fr = 0.2$. Whereas the trajectories of PPG and P2G both essentially matched the FB trajectory for $Ro = Fr = 0.1$ and for times $t < 100$, here we begin to see differences in the trajectories for $t > 30$, with P2G more accurate for $t > 30$. Furthermore, we can also see differences in the speeds at which each dipole is moving. At time $t = 100$, the path lengths are 4.91 (FB), 4.93 (P2G), 5.75 (PPG) and 5.28 (QG). The speed of propagation for P2G is the closest to that of FB, whereas PPG and QG overestimate the speed.

Next we investigate how well the models PPG and P2G are able to reproduce the trapping of gravity waves inside the dipole as has been observed (Snyder *et al.* 2007; Viúdez 2007; McIntyre 2009). Figure 8 shows the vertical velocity averaged over the time interval $10 \leqslant t \leqslant 20$, with light grey shading for values $w \in [-0.5, -0.05]$, and darker grey to denote $w \in [0.05, 0.5]$. A quasi-stationary wave pattern is clearly evident in the FB (figure 8*a*) and P2G (figure 8*b*) systems, though the P2G and FB patterns differ in details. However, this quasi-stationary oscillation toward the jet exit is completely lacking in the PPG model (figure 8*c*). As will be further illustrated below, the PPG vortical–vortical–wave interactions drain energy from the vortical flow component; their feedback onto the vortical modes is not enough to contribute substantially to the formation of new coherent structures.

Figure 9 shows the vertical vorticity $\omega = \partial_x v - \partial_y u$ at $t = 90$ for P2G (9*a*,*c*) and PPG (9*b*,*d*) when the initial conditions consist of an initial balanced dipole (9*a*,*b*), and the balanced dipole plus wave noise (9*c*,*d*). In the run with wave noise added, the wave noise spectrum as a function of wavenumber has the form

$$F(k) = \epsilon_f \frac{\exp(-0.5(k - k_f)^2/\gamma)}{\sqrt{2\pi\gamma}}. \tag{4.9}$$

Here the standard deviation is $\gamma = 25$, the amplitude is $\epsilon_f = 0.022$, and the peak wavenumber is $k_f = 15$. Each of the vortical, + wave and − wave energies is about

https://doi.org/10.1017/jfm.2014.138 Published online by Cambridge University Press

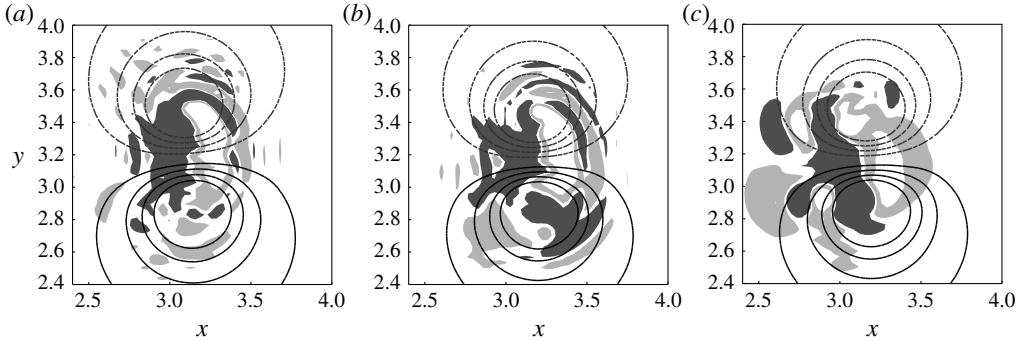


FIGURE 8. $Fr = Ro = 0.2$. Vertical velocity at $z = \pi$ and averaged over the interval $t \in [10, 20]$ for (*a*) FB, (*b*) P2G and (*c*) PPG. The light grey shade is associated with negative vertical velocities with values in the range $w \in [-0.5, -0.05]$. The darker grey area is associated with positive vertical velocities in the range $w \in [0.05, 0.5]$. Contours of streamfunction ψ are also included.

1/3 of the total energy in the system. For both runs, with and without wave noise, one can observe a strong wake following the PPG dipole (figure 9*b*,*d*). As will be verified in § 5, the PPG wakes indicate that the vortical–vortical–wave interactions act as an efficient sink of energy from vortical to wave modes, but allow only for an extremely slow leak of energy back from wave to vortical modes. Despite the energy sink from vortical to wave modes, the trajectory of the PPG dipole stays remarkably close to the FB trajectory for long times. By contrast, the P2G dipole has a much smaller amplitude wake, especially for the run without additional wave noise. We will see in § 5 that the vortical–wave–wave interactions included in the P2G model allow for more transfer of energy from wave to vortical modes, and that these interactions are necessary for the generation of coherent structures.

To summarize § 4, we studied the effects of wave–vortical interactions for the evolution of an initially balanced dipole. In the full Boussinesq system, there is a cyclonic drift away from the QG trajectory as well as a decrease in dipole speed from the QG speed (for larger $Ro = Fr$). Additionally, the structure of the dipole is modified, toward the jet exit region, to include a quasi-stationary wave pattern in the vertical velocity moving at the speed of the dipole (Snyder *et al.* 2007). The PPG model (adding vortical–vortical–wave interactions to QG) performs significantly better than the FL model in capturing the long-time speed and trajectory of the dipole, especially at the larger $Ro = Fr = 0.1, 0.2$. The good agreement of PPG for dipole speed/trajectory may be somewhat surprising, given that the PPG wake is too strong (figure 9). The pronounced PPG wake indicates that the vortical–vortical–wave interactions act mainly as a sink of energy from vortical to wave modes, as will be elaborated further in § 5. The P2G model (adding vortical–wave–wave interactions to PPG) is of course even more accurate than PPG for tracking the speed and trajectory of the FB dipole, and only shows significant deviation at long times when the Rossby and Froude numbers are greater than approximately $Ro = Fr > 0.2$ (figure 7). It has been demonstrated that the vortical–wave–wave interactions of P2G are necessary to capture the vertical structure of the adjusted dipole in the form of a quasi-stationary oscillation at the front of the jet exit region (figure 8).

https://doi.org/10.1017/jfm.2014.138 Published online by Cambridge University Press

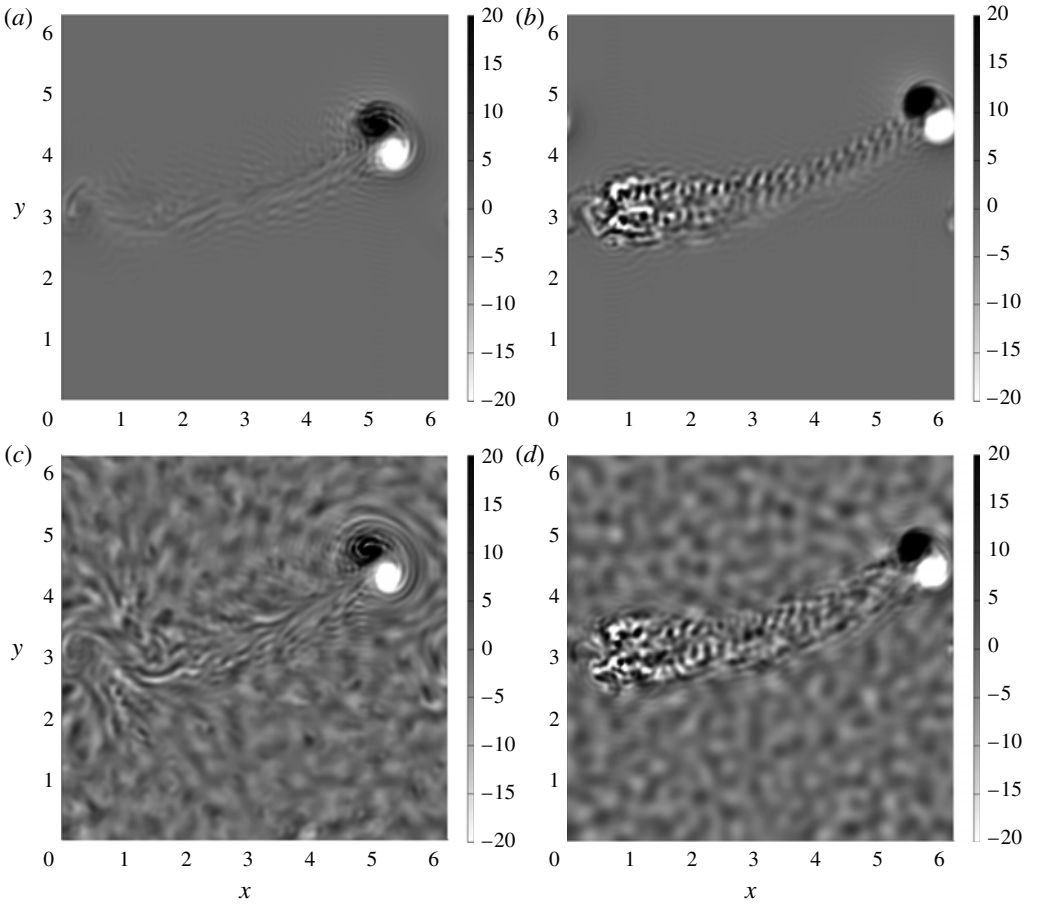


FIGURE 9. $Fr = Ro = 0.2$. Contours of vertical vorticity at $z = \pi$, $t = 90$ for (a,c) P2G and (b,d) PPG for an initially balanced dipole (a,b), and the balanced dipole plus wave noise (c,d). At the initial time, the dipole location is shifted to the left boundary.

5. Random decay simulations

Following up on the dipole simulations, here we explore which class(es) of interactions are associated with transfer of energy from vortical to wave modes and vice versa, as well as which class(es) of interactions are primarily responsible for the generation of coherent structures. Praud, Sommeria & Fincham (2007) performed an experimental study of decaying grid turbulence for a range of initial Rossby and Froude numbers. They studied differences from QG for their higher Rossby numbers, including the change from statistical symmetry of emerging cyclones and anticyclones for small Ro, to cyclone dominance at moderate Ro. Energy spectra and structure formation have also been studied extensively in both decaying and forced numerical simulations, and although we do not provide a comprehensive review, some examples are Metais *et al.* (1996), Smith & Waleffe (2002), Waite & Bartello (2006) and Deusebio, Vallgren & Lindborg (2013); see also references therein. The experimental and numerical evidence consistently shows that (i) rotation inhibits the rate of kinetic energy decay leading to a transfer of energy from small to large scales, and (ii) the

https://doi.org/10.1017/jfm.2014.138 Published online by Cambridge University Press

aspect ratio H/L of emerging structures is small in stratification-dominated flows and large in rotation-dominated flows, where H (L) is the height (horizontal length) of the structures. Three representative cases are considered in the following sections: rotating stratified turbulence with $Ro = Fr = 0.2$, rotation-dominated turbulence with $Ro = 0.1$, $Fr = 1$, and stratification-dominated turbulence with $Ro = 1$, $Fr = 0.1$. For these moderate parameter values, we are interested in identifying which models/interactions are able to develop structures, and if the details of the results are statistically similar to those given by the full Boussinesq system.

There are of course a multitude of possible setups to study structure formation, and here we choose most runs to start from random initial conditions with energy in the vortical modes. The initial vortical spectrum as a function of wavenumber has the Gaussian form

$$F(k) = \epsilon_f \frac{\exp(-0.5(k-k_f)^2/\gamma)}{\sqrt{2\pi\gamma}}, \tag{5.1}$$

where $\gamma = 100$, $\epsilon_f = 0.16$, and $k_f = 15$. Later in § 5.4, we also consider a complementary run starting from completely unbalanced initial conditions (energy only in the wave modes) in order to focus on the transfer of energy from wave modes to vortical modes. In the latter case, each $\pm$ wave-mode spectrum as a function of the wavenumber is given by (5.1).

The characteristic scales have been chosen as $[U] = \|u_{t=0}\|_{L^2}$, $[L] = L/k_f$, $T_i = [L]/[U]$, where $L = 2\pi$ is the size of the box. As in § 4, the initial time scale T_i will be used to rescale the time $t' = t/T_i$ and the prime will be dropped. The end time for simulations ranges from 100 to 500 time units, depending on the test case. The Froude and Rossby numbers are computed at each time step as

$$Fr(t) = \frac{\|\boldsymbol{u}\|_{L^2}}{N[L]}, \quad Ro(t) = \frac{\|\boldsymbol{u}\|_{L^2}}{f[L]}. \tag{5.2a,b}$$

In random decay simulations of the full Boussinesq system and the intermediate models, the Froude and Rossby numbers decrease roughly by a factor of three before reaching a statistically quasi-steady state. This decay in Ro and Fr was also noted in Metais *et al.* (1996), where Ro and Fr decreased by a factor of 10 after 255 of their time units. The decay in Ro and Fr is much less in the QG model without wave modes, since the bulk of the QG energy is transferred upscale by the vortical modes. The buoyancy frequency f and Coriolis parameter N are chosen so that Ro and Fr for the FB model reach the value of $Fr = Ro \approx 0.2$ for the rotating stratified simulations (§ 5.1), $Ro \approx 0.1$, $Fr \approx 1$ for the rotation-dominated turbulence simulations (§ 5.2), and $Ro \approx 1$, $Fr \approx 0.1$ for the stratification-dominated turbulence case (§ 5.3). Since we are matching initial conditions, this necessarily means that the QG Ro and Fr will be larger than the corresponding runs for FB and the wave–vortical reduced models.

5.1. *Rotating stratified decay for $Ro \approx Fr \approx 0.2$; initial energy in the vortical modes*

The random initial conditions in this simulation give the following characteristic scales: $[U] = 1.28$, $[L] = 0.42$, $T_i = 0.33$. The values $f = N = 3.5$ lead to $Ro = Fr = 0.2$ by the end of the FB simulation, as computed by (5.2). Figure 10 shows the vertical vorticity contours at time $t = 100$ and vertical height $z = \pi$. One observes that the FB and P2G results are similar in terms of number of vortices in the domain, the characteristic

https://doi.org/10.1017/jfm.2014.138 Published online by Cambridge University Press

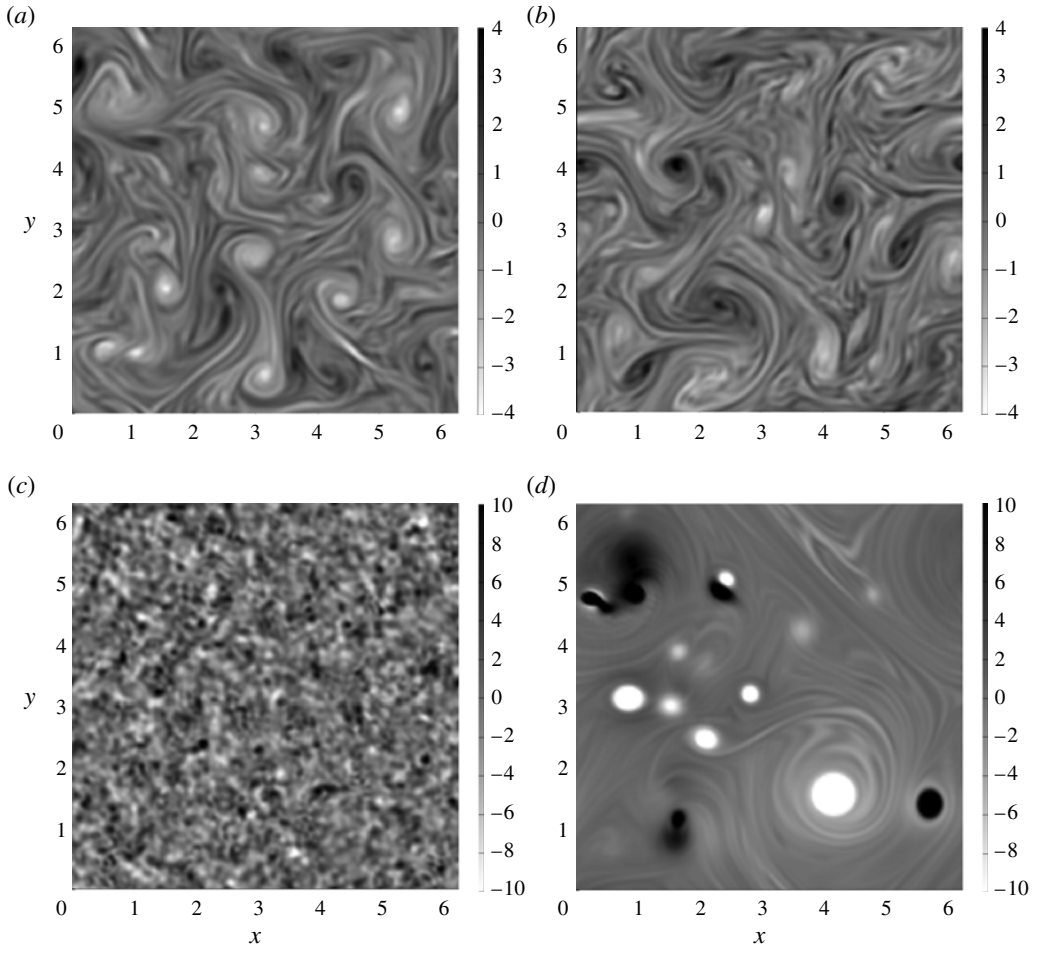


FIGURE 10. Rotating stratified turbulence: $Fr = Ro \approx 0.2$. Vertical vorticity at $z = \pi$, $t = 100$ for (*a*) FB, (*b*) P2G, (*c*) PPG, and (*d*) QG. Note that FB and P2G have a different colour scale from PPG and QG.

size and strength of the vortices, and the fine-scale structure. The maximum absolute vertical vorticity is 5.7 for FB and 8.1 for P2G. In contrast the PPG vorticity has a maximum of 24.9 and does not form vortices of scale larger than the scale $[L] = 0.42$ associated with the initial conditions. As discussed below, the vortical–vortical–wave interactions act as an efficient sink of energy from vortical to wave modes, but allow only for an extremely slow leak of energy back from wave to vortical modes. The QG vorticity is much stronger than any of the other models with a maximum of 162.6. Figure 11 presents the probability density function of vertical vorticity for each of the models. The data for figures 11(*a*) and 11(*b*) are the same, and 11(*b*) is simply a close-up of the p.d.f.s in the vorticity range $[-15, 15]$. The exponential tails of the QG model extending to large absolute vorticity values are absent from the other models. Below we sometimes present p.d.f. data in close-up views, but keeping in mind the broad tails of the QG model. At time $t = 100$, the p.d.f.s for all the runs QG, PPG, P2G and FB appear symmetric, as is expected for $Ro = Fr$ (e.g. Praud *et al.* 2007).

https://doi.org/10.1017/jfm.2014.138 Published online by Cambridge University Press

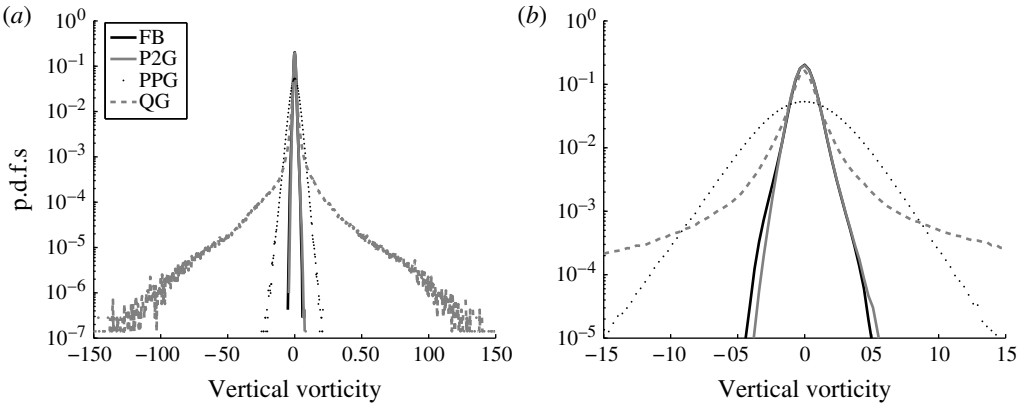


FIGURE 11. Rotating stratified turbulence: $Fr = Ro \approx 0.2$. Probability distribution functions (p.d.f.s) of vertical vorticity at $t = 100$. The data for the two plots is the same, and (*b*) is a close-up of (*a*) in the vorticity range $[-15, 15]$.

In regimes where rotation is strong, the centroid

$$\mathrm{Cent}(t) = \frac{\sum_{\boldsymbol{k}} k(|u_{\boldsymbol{k}}|^2 + |v_{\boldsymbol{k}}|^2 + |w_{\boldsymbol{k}}|^2)}{\sum_{\boldsymbol{k}} (|u_{\boldsymbol{k}}|^2 + |v_{\boldsymbol{k}}|^2 + |w_{\boldsymbol{k}}|^2)} \tag{5.3}$$

is roughly associated with the inverse-size of the emerging vortices (e.g. see Remmel *et al.* 2013). Here $(u_{\boldsymbol{k}}, v_{\boldsymbol{k}}, w_{\boldsymbol{k}})$ is the Fourier amplitude associated with the vector $\boldsymbol{k}$ and $k = |\boldsymbol{k}|$. The centroid reflects vortex size information but does not contain the amplitude information in figures 10 and 11. This statistic is shown in figure 12, where it is clear that QG leads to the largest vortices, and that the vortices of P2G and FB are close to each other in size. At $t = 100$, the centroid values are 1.82 (QG), 5.38 (P2G), 4.84 (FB) and 19.6 (PPG).

To further quantify the information contained in figures 10–12, we next investigate spectra, which also indirectly provide information about the transfer of energy between wave modes and vortical modes. Figure 13 shows the vortical (13*a*,*b*) and wave (13*c*,*d*) spectra at times $t = 10$ (13*a*,*c*) and $t = 100$ (13*b*,*d*). The grey circles denote the initial vortical-mode spectrum. Here we focus on the overall differences between the models as opposed to scaling laws of any individual model (which are not measured precisely using our moderate resolution of 192^3). The transfer of vortical-mode energy to large scales by the (000) interactions of the QG model is evident, and of course there is no energy in wave modes (which are excluded from the QG model). Compared to the FB and P2G runs, the high values of QG energy at low wavenumbers indicate larger and stronger vortices as in figures 10–12. In the PPG model, there is a drastic effect of adding the (00±) to the QG (000) interactions. PPG clearly transfers a large amount of energy from vortical modes to wave modes during the earlier times of the simulation: integrating over wavenumbers $5 \leqslant k \leqslant 50$ at $t = 10$, the ratio of the PPG wave energy to the PPG vortical-mode energy is roughly 7. From $t = 10$ to $t = 100$, the PPG spectra suggest very little (if any) transfer of energy back from wave modes to vortical modes (see also Bartello 1995). Following

https://doi.org/10.1017/jfm.2014.138 Published online by Cambridge University Press

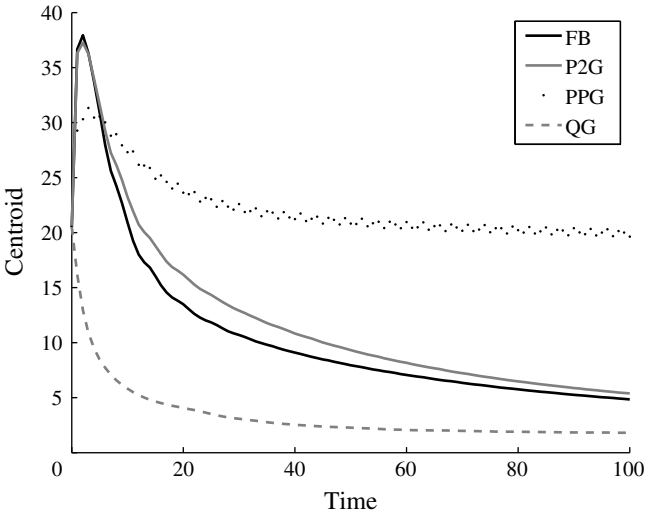


FIGURE 12. Centroid versus time in rotating stratified turbulence with $Fr = Ro \approx 0.2$.

the energy drain from vortical to wave modes in PPG, it appears that the (000) interactions are ineffective at transferring energy to large scales.

The vortical-mode spectrum of the P2G model (adding $(0 \pm \pm)$ interactions to PPG) is almost overlapping the FB spectra at both times $t = 10$ and $t = 100$, with small differences at large k for $t = 10$, and at intermediate k for $t = 100$. Comparing the times $t = 10$ and $t = 100$ for both P2G and FB, one sees that there is (i) transfer of energy from wave modes to vortical modes, and (ii) growth of energy in the low-wavenumber vortical modes. The transfer of energy by QG (000) interactions was drained by the $(00\pm)$ interactions of PPG, but is partially reconciled by the addition of the $(0 \pm \pm)$ interactions in P2G. Therefore it is clear that the $(0 \pm \pm)$ interactions are necessary to achieve the correct balanced end state. For later times (see figure 13*d*), the lack of three-wave $(\pm \pm \pm)$ interactions in P2G results in higher wave energy at all scales as compared to FB, but apparently without a significant impact on structure formation in the current decay runs (see Smith & Waleffe 1999, 2002; Laval, McWilliams & Dubrulle 2003; Smith & Lee 2005; Waite & Bartello 2006; Remmel *et al.* 2013, for effects of three-wave interactions in forced flows). Since three-wave interactions support their own forward transfer to small scales where energy is dissipated, the wave energy of PPG is approximately 1.6 higher than the wave energy of FB at time $t = 100$ (see also Remmel *et al.* 2010). The trends observed in figure 13 were also observed for the parameter regimes considered in §§ 5.2 and 5.3; the spectra for the runs presented in §§ 5.2 and 5.3 will not be shown for conciseness of the presentation.

Altogether, the vertical vorticity contours and p.d.f.s, centroid data and spectra suggest the following: $(00\pm)$ interactions are mainly a sink of energy from vortical modes to wave modes; $(0 \pm \pm)$ interactions transfer energy from wave modes to vortical modes; $(00\pm)$ and $(0 \pm \pm)$ interactions together provide two-way feedback between waves and vortical modes, allowing for the simultaneous formation of large-scale coherent structures and the development of 3D fine-scale structure, which are quantitatively similar to the full Boussinesq simulations; $(\pm \pm \pm)$ play a lesser role, at least for moderate $Ro \approx Fr$. Smith & Waleffe (2002) showed that exact three-wave resonances are not possible for $1/2 \leqslant f/N \leqslant 2$, and thus the role of

https://doi.org/10.1017/jfm.2014.138 Published online by Cambridge University Press

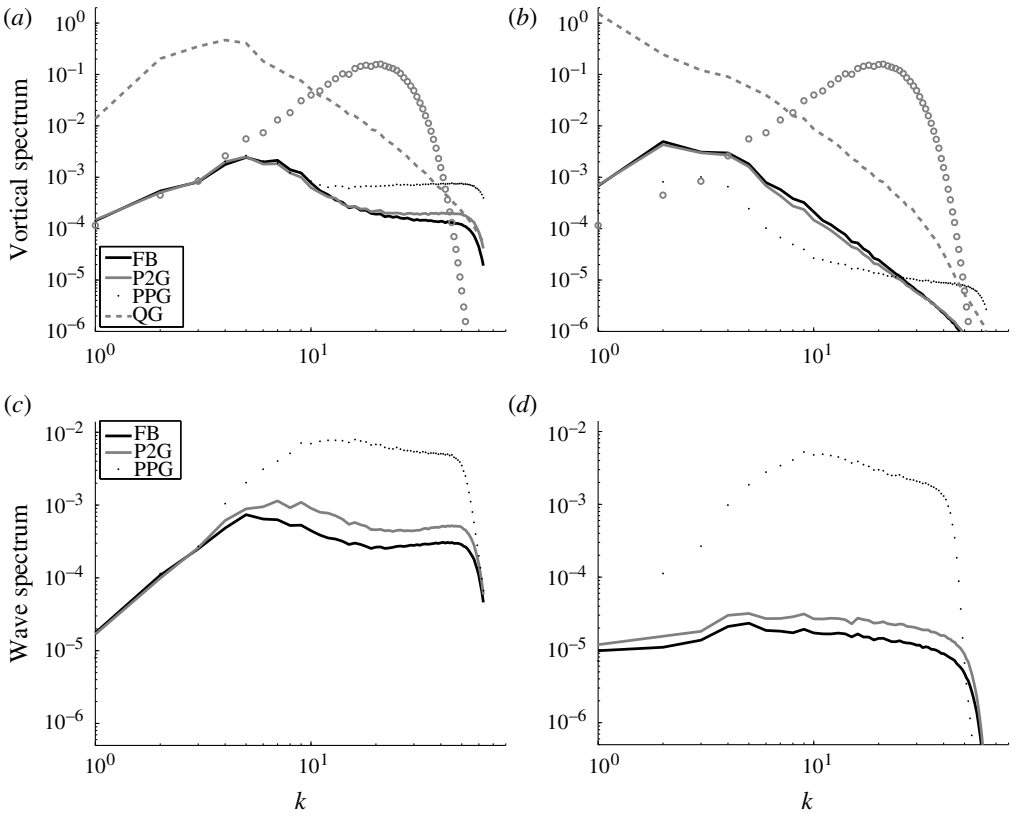


FIGURE 13. Rotating stratified turbulence: $Fr = Ro \approx 0.2$. (*a*,*b*) Vortical and (*c*,*d*) wave spectra at times $t = 10$ (*a*,*c*) and $t = 100$ (*b*,*d*). The grey circles denote the initial vortical spectrum.

three-wave near resonances is also likely to be diminished in this range of f/N. We caution that three-wave near resonances are known to be important in forced flows on long time scales in the rotation-dominated and buoyancy-dominated cases, where they contribute to the generation of cyclonic vortical columns and vertically sheared horizontal flows, respectively (see Smith & Waleffe 1999, 2002; Laval *et al.* 2003; Smith & Lee 2005; Waite & Bartello 2006; Remmel *et al.* 2013, for effects of three-wave interactions in forced flows). In §§ 5.2 and 5.3, we explore the PPG and P2G models in representative rotation-dominated- and stratification-dominated-decay runs.

5.2. *Rotation-dominated decay for* $Ro \approx 0.1$, $Fr \approx 1$*; initial energy in the vortical modes*

It is well-documented that rotation inhibits the decay of kinetic energy, coincident with energy transfer from small to large scales (e.g. Cambon, Mansour & Godeferd 1997; Praud *et al.* 2007). For moderate Rossby numbers, the accumulation of energy at large scales is associated with vortical columns which are predominantly cyclonic (Hopfinger *et al.* 1982; Smith & Waleffe 1999; Bourouiba & Bartello 2007; Praud *et al.* 2007). Here we test the robustness of the results from the previous section,

https://doi.org/10.1017/jfm.2014.138 Published online by Cambridge University Press

by investigating the PPG and P2G models for a rotation-dominated case in which the Rossby number is an order of magnitude smaller than the Froude number. We again compare these models to the full Boussinesq dynamics as well as QG dynamics. Embid & Majda (1998) showed that QG is rigorously derived in the limit $Ro \sim Fr = \epsilon \to 0$, and this condition is not satisfied with Ro smaller than Fr by an order of magnitude. Recognizing this limitation, here we interpret the QG model simply as the bottom of the model hierarchy presented in table 1. The random initial conditions in this simulation give the following characteristic scales: $[U] = 0.59$, $[L] = 0.42$, $T_i = 0.72$. With $f = 10$ and $N = 1$, the Froude and Rossby numbers computed by (5.2) for the FB model are approximately $Fr \approx 1$, $Ro \approx 0.1$ by the end of the simulation.

Vertical vorticity contours at $z = \pi$ for the different models are shown in figure 14. One observes again that the PPG model is not able to form coherent structures, and that P2G and FB have similar vertical vorticity structure. As expected, the P2G and FB simulations lead to a larger number of smaller and less intense vortices compared to the QG simulation. The minimum and maximum vorticity values at time $t = 100$ are $[-7.2, 18.2]$ (FB), $[-8.8, 21.6]$ (P2G), $[-57.0, 55.2]$ (PPG) and $[-93.6, 90.9]$ (QG). A close-up view of the vertical vorticity p.d.f.s in the vorticity range $[-20, 20]$ is shown in figure 15(*a*), and one can see the beginnings of the broad tails associated with QG. At $t = 100$, there is a strong positive skewness associated with the p.d.f.s of P2G and FB. The vertical vorticity skewness as a function of time

$$\mathrm{Skew}(\omega) = \frac{\displaystyle\int_V \omega^3 \mathrm{d}V}{\left(\displaystyle\int_V \omega^2 \mathrm{d}V\right)^{3/2}} \tag{5.4}$$

is plotted in figure 15(*b*), where $\omega = \partial_x v - \partial_y u$ is the vertical vorticity. The monotonically increasing skewness of P2G and FB reflects a growing predominance of cyclones. Note that the P2G skewness is always larger than the FB skewness, indicating that three-wave interactions systematically reduce the asymmetry. Section 5.4 provides further evidence that the vortical–wave–wave interactions are solely responsible for vorticity asymmetry. The centroid defined by (5.3) is shown in figure 16 for FB, P2G, and QG and verifies the smaller vortices associated with P2G and FB as compared to QG. At time $t = 100$, the centroid values are 3.53 (FB), 3.9 (P2G), and 2.57 (QG). To check for vertical coherence of the QG, P2G and FB vortices, figure 17 shows vertical vorticity contours with values $\pm 10\,\%$ of the maximum value in the entire $2\pi \times 2\pi \times 2\pi$ periodic domain (time $t = 100$; PPG is not shown since it does not generate large-scale vortices). It is evident that all the models (except for PPG) form vertically coherent vortices.

5.3. *Stratification-dominated decay for $Ro \approx 1$, $Fr \approx 0.1$; initial energy in the vortical modes*

Pancake vortices and horizontal layers are well-known to form when stratification is the dominant effect (see e.g. Waite & Bartello 2006; Praud *et al.* 2007, and references therein). Here we consider a buoyancy-dominated case with $Ro \approx 1$, $Fr \approx 0.1$ to confirm that P2G forms flattened large-scale structures similar to the full Boussinesq system. We verified that PPG does not form structures larger than the characteristic length scale given by the initial conditions, but we do not show these plots since

https://doi.org/10.1017/jfm.2014.138 Published online by Cambridge University Press

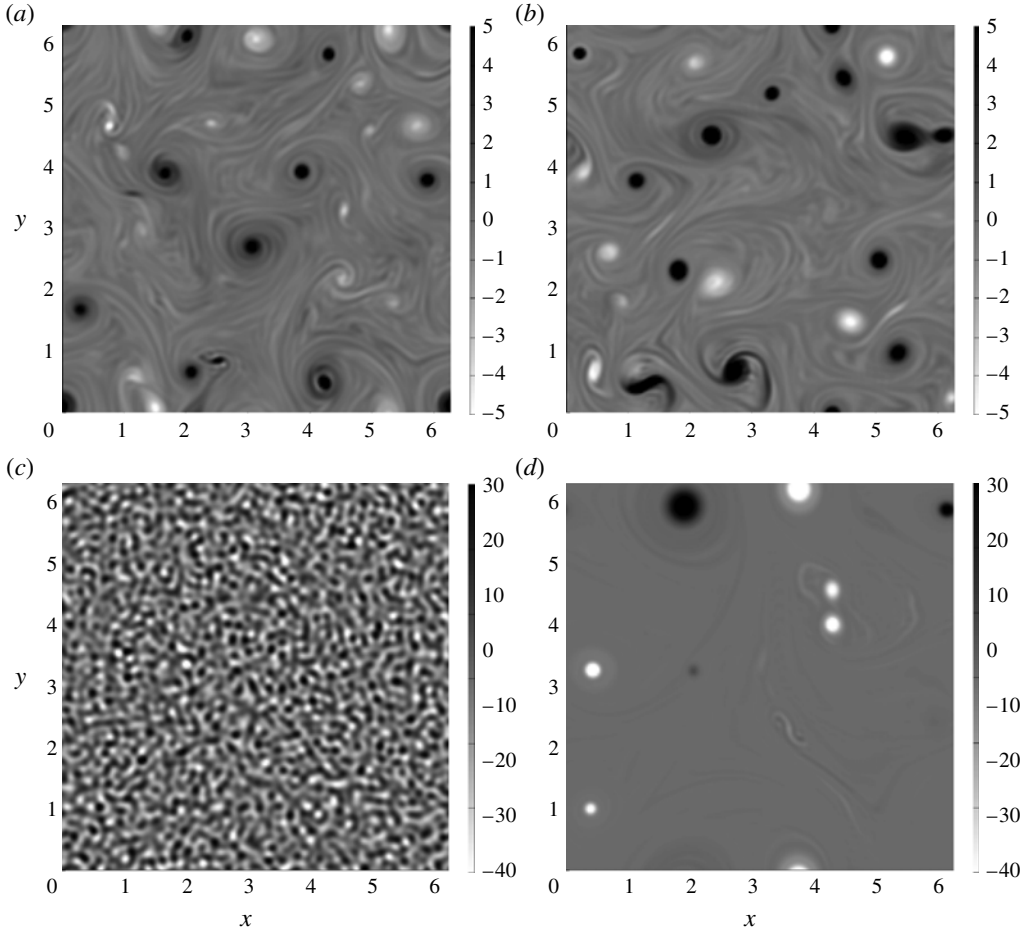


FIGURE 14. Rotation-dominated turbulence: $Ro \approx 0.1$, $Fr \approx 1$. Vertical vorticity at $z = \pi$, $t = 100$ for (*a*) FB, (*b*) P2G, (*c*) PPG, and (*d*) QG. Note that FB and P2G have a different colour scale from PPG and QG.

they are rather uninteresting. In these simulations, the characteristic scales are $[U] = 1.55$, $[L] = 0.42$, $T_i = 0.27$ and the frequencies are $f = 1$, $N = 10$.

Figure 18 shows FB and P2G contours of vertical vorticity with values $\pm 30\%$ of the maximum value attained at $t = 500$. The minimum and maximum vertical vorticity values at time $t = 500$ are $[-3.1, 4.4]$ (FB) and $[-3.5, 4.3]$ (P2G). We have verified with spectra (not shown) that the vortical-mode energy dominates over wave-mode energy, and that the largest amount of vortical-mode energy is in wavenumber $k_h = 1$. Even in the FB simulation, there is not a dominance of the vertically sheared horizontal flows ($k_h = 0$ wave modes) in this unforced case, presumably because there are no special near-resonant three-wave interactions excited involving a forced wavenumber. From spectra, the main effect of the three-wave interactions energetically is to reduce the amplitude of the wave-mode spectrum at all k values for FB compared to P2G.

https://doi.org/10.1017/jfm.2014.138 Published online by Cambridge University Press

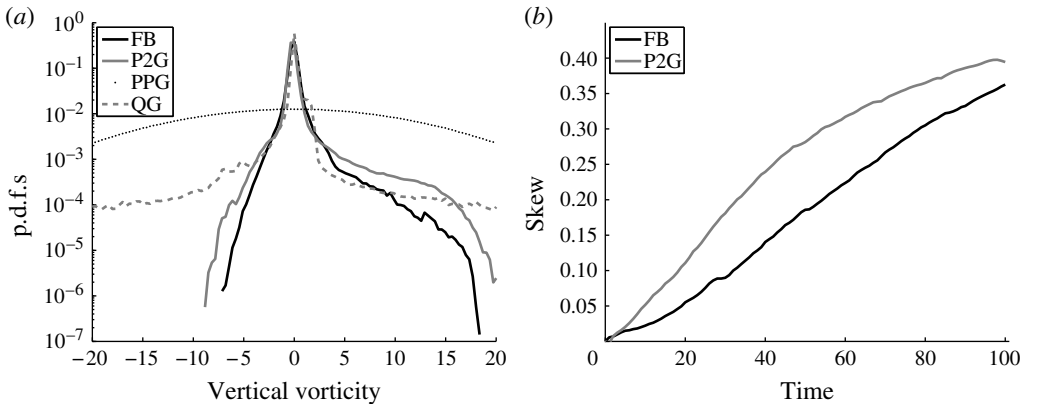


FIGURE 15. Rotation-dominated turbulence: $Ro \approx 0.1$, $Fr \approx 1$. (*a*) Close-up view of the p.d.f.s of vertical vorticity at time $t = 100$. (*b*) Skewness of the vertical vorticity versus time.

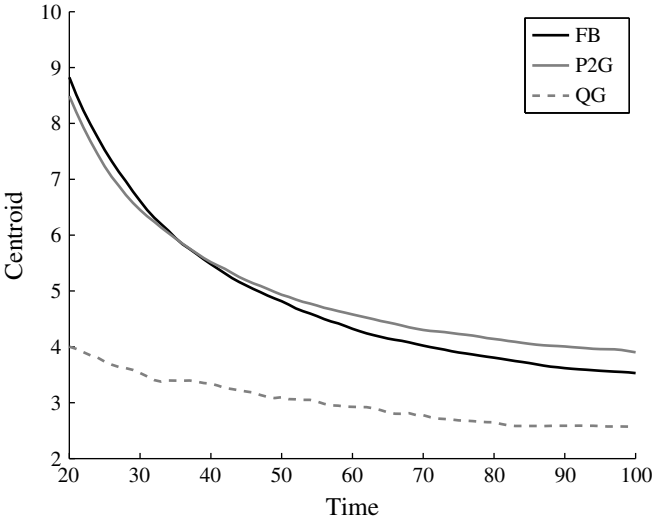


FIGURE 16. Centroid versus time in rotation-dominated turbulence with $Ro \approx 0.1$, $Fr \approx 1$.

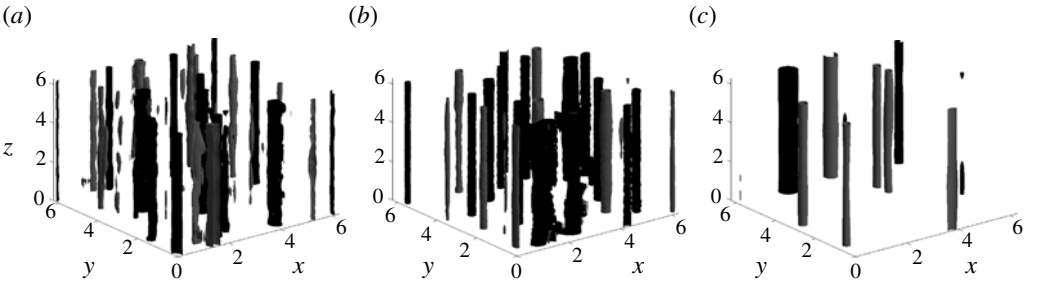


FIGURE 17. Rotation-dominated turbulence: $Ro \approx 0.1$, $Fr \approx 1$. Vorticity contours $\pm 10\,\%$ of the maximum value at $t = 100$ for (*a*) FB, (*b*) P2G, and (*c*) QG.

https://doi.org/10.1017/jfm.2014.138 Published online by Cambridge University Press

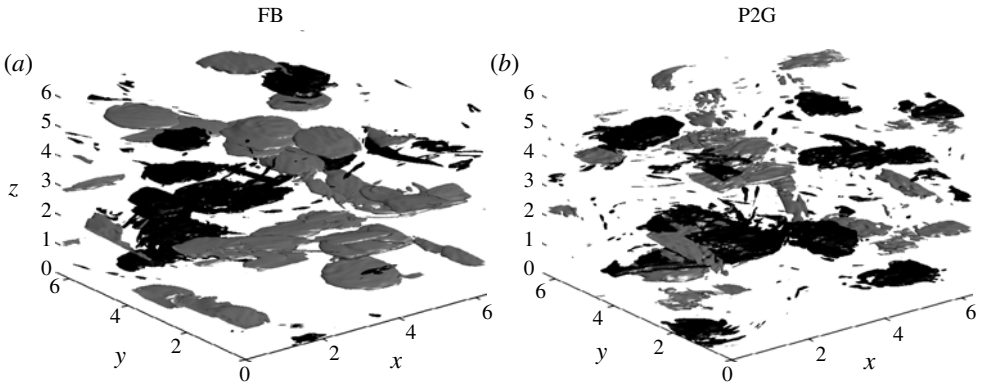


FIGURE 18. Strongly stratified turbulence: $Fr \approx 0.1$, $Ro \approx 1$, $t = 500$. Vertical vorticity contours at $\pm 30\%$ of the maximum value attained by the FB model at this time for (*a*) FB and (*b*) P2G (black is positive, grey is negative).

5.4. *Rotating stratified decay for $Ro = Fr \approx 0.1$; initial energy in the wave modes*

The simulations presented in this section have initial energy only in the wave modes. With zero initial energy in the vortical modes, the vortical-mode energy of the PPG model (with (000) and (00±) and all permutations) remains zero for all time and only the phases of the wave modes will change. Thus, in this case, it is interesting to consider the reduced model consisting of (000) and (0 ± ±) interactions (and all permutations), which we denote P2SG (not included in table 1). As in the full Boussinesq system, both reduced models P2G and P2SG create vortices; the P2SG vortices are larger and more intense than the P2G and FB vortices because of the absence of the (00±) interactions which drain energy from the vortical modes and thereby make the inverse energy transfer less efficient. While the P2G and FB vertical vorticity p.d.f.s are roughly symmetric, the P2SG run leads to positively skewed p.d.f.s, linking the (0 ± ±) directly to cyclone dominance.

Initially, each ± wave spectrum as a function of the wavenumber is given by (5.1). The initial conditions have characteristic scales $[U] = 1.28$, $[L] = 0.42$, $T_i = 0.33$, and the choice $f = N = 7$ leads to $Ro = Fr \approx 0.1$ by the end of the FB simulation. Figure 19 shows contours of the vertical vorticity for FB (19*a*), P2G (19*b*), PPG (19*c*) and P2SG (19*d*) at $t = 100$. PPG does not form vortices larger than $[L] = 0.42$ ($2\pi/k_f$ in (5.1)). As in § 5.1, the FB and P2G simulations produce a statistically equal number of larger-scale cyclones and anticyclones evolving in a sea of elongated vortex filaments. There are fewer stronger vortices in the P2SG run, with a clearly visible preference for cyclones. The minimum and maximum vertical vorticity values at time $t = 100$ are $[-11.3, 8.9]$ (FB), $[-7.3, 10.2]$ (P2G), $[-86.4, 82.6]$ (PPG) and $[-12.4, 46.4]$ (P2SG). The full p.d.f.s at time $t = 100$ are given in figure 20. The p.d.f. of the PPG model is essentially the same as the p.d.f. of vertical vorticity corresponding to the structureless initial conditions, with large standard deviation compared to the p.d.f.s of FB and P2G. For the P2SG model, the p.d.f. tail on the positive vorticity side corroborates the dominance of cyclones observed in figure 19. The skewness (5.4) increases in time for P2SG, with values 1.2×10^{-5} ($t = 0$), 8.6×10^{-2} ($t = 20$), 1.6×10^{-1} ($t = 40$), 2.3×10^{-1} ($t = 60$), 2.8×10^{-1} ($t = 80$) and 3.3×10^{-1} ($t = 100$). This numerical evidence indicates that the vortical–wave–wave interactions are responsible for the positive skewness in the Boussinesq system when rotation is important.

https://doi.org/10.1017/jfm.2014.138 Published online by Cambridge University Press

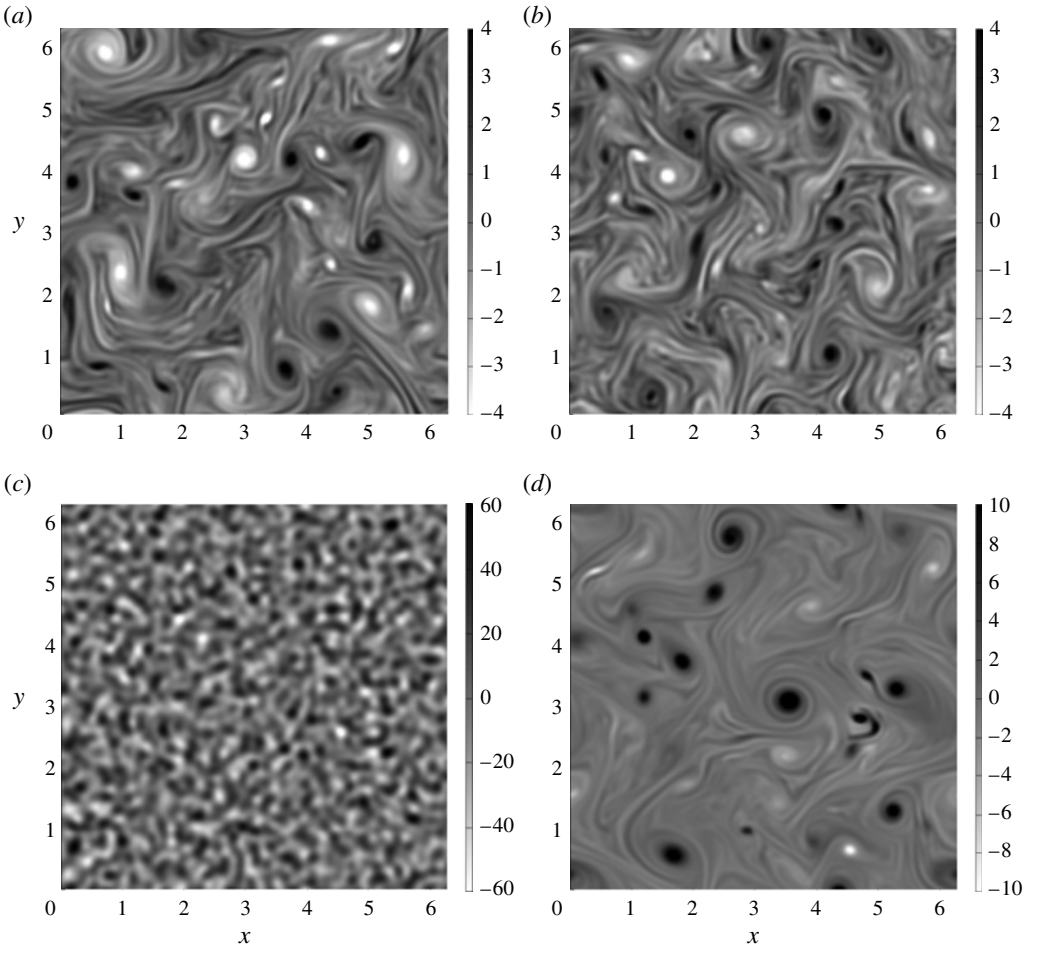


FIGURE 19. Rotating stratified turbulence with $Fr = Ro \approx 0.1$, starting from energy in the wave modes. Vertical vorticity at $z = \pi$ at time $t = 100$ for (*a*) FB, (*b*) P2G, (*c*) PPG, and (*d*) P2SG. Note the different colour scales.

Figure 21 shows the vortical (21*a*,*b*) and wave (21*c*,*d*) spectra at $t = 10$ (21*a*,*c*) and $t = 100$ (21*b*,*d*). The vortical-mode spectrum is initially null in this set of runs. The dotted line in figure 21(*c*,*d*) is the PPG wave spectrum, which coincides with the initial spectrum at all but the largest wavenumbers, because the PPG spectrum is not changing apart from a small amount of dissipation by the hyperviscosity. As discussed above, only the phases of the wave modes change for the PPG model with initial conditions that project onto the wave modes only. In all of the other models P2SG, P2G and FB, we observe a strong transfer of energy from the wave modes to the vortical modes; the latter transfer is most efficient in the P2SG model because of the absence of the (00±) interactions. Since the P2SG vortical modes receive and retain more of the initial energy, the P2SG model also exhibits more efficient transfer of energy to large-scale vortices by the (000) modes. By $t = 100$, the peak of the P2SG vortical-mode spectrum has a higher value at a lower wavenumber than the corresponding spectral peaks of P2G and FB, reflecting stronger and larger vortices. At both early time $t = 10$ and late time $t = 100$, the P2G and FB vortical-mode spectra

https://doi.org/10.1017/jfm.2014.138 Published online by Cambridge University Press

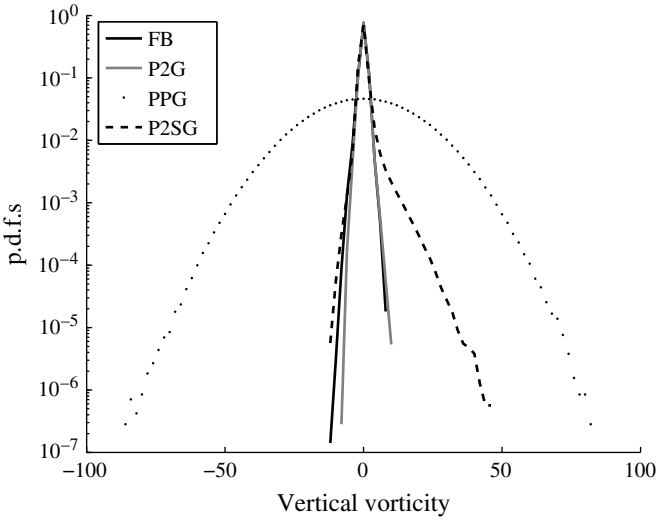


FIGURE 20. Rotating stratified turbulence: $Fr = Ro \approx 0.1$, with random initial conditions in the wave modes. P.d.f.s of vertical vorticity at $t = 100$.

are quantitatively very similar. The wave spectrum of P2G is systematically higher in energy for all wavenumbers than the FB wave spectrum because the three-wave interactions support their own forward cascade of energy to small scales (Remmel *et al.* 2010, 2013).

6. Summary and discussion

Using a class of reduced models, we have studied two-way feedback between wave modes and vortical modes of the rotating Boussinesq equations. The models were described in physical space as coupled sub-systems for the vortical mode and wave modes, and by projections of the nonlinear terms to select specific classes of wave–vortical interactions. The four models QG, PPG, P2G and FB in table 1 form a model hierarchy. QG is at the base including only vortical–vortical–vortical (000) interactions. PPG is a correction to QG with two-way feedback including vortical–vortical–vortical (000) and vortical–vortical–wave interactions (00±), and is closely related to the first-order PV-inversion model of Muraki *et al.* (1999). The P2G model is almost complete, including vortical–vortical–vortical (000), vortical–vortical–wave (00±) and vortical–wave–wave (0 ± ±) coupling (excluding only three-wave (± ± ±) interactions). P2G extends a forced linear FL model to include two-way feedback instead of one-way feedback between the vortical and wave modes. Note that our FL model is a simplified version of the FL model studied in Snyder *et al.* (2009). Finally the full Boussinesq FB model includes all possible interaction classes.

For evolution of an initially balanced dipole in the full Boussinesq system, there is a cyclonic drift from the QG trajectory as well as a decrease in dipole speed from the QG speed (for larger $Ro = Fr$). Additionally, the structure of the dipole is modified, toward the jet exit region, to include a quasi-stationary wave pattern in the vertical velocity moving at the speed of the dipole (Snyder *et al.* 2007). An FL model with one-way feedback from vortical modes to wave modes is able to track the dipole

https://doi.org/10.1017/jfm.2014.138 Published online by Cambridge University Press

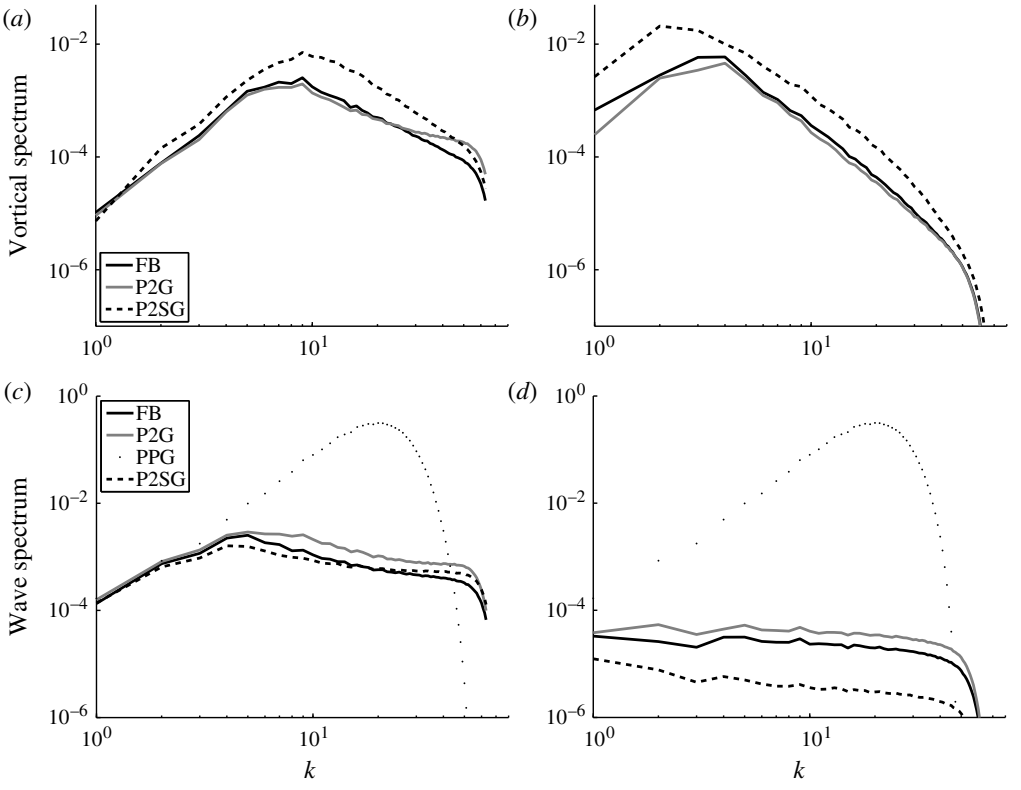


FIGURE 21. Stratified rotating turbulence: $Fr = Ro \approx 0.1$, with unbalanced initial conditions. (*a*,*b*) Vortical and (*c*,*d*) wave spectrum at times $t = 10$ (*a*,*c*) and $t = 100$ (*b*,*d*).

trajectory for relatively short times at small Rossby and Froude numbers (for times up to $t \approx 10$ in our time units at $Ro = Fr = 0.1$). For the same $Ro = Fr = 0.1$, the PPG model accurately tracks the dipole for approximately 10 times longer (figure 5). For simply tracking the speed and trajectory of the dipole, the vortical–wave–wave interactions of P2G are not necessary to provide a significant improvement upon PPG except for the largest of our Rossby and Froude numbers $Ro = Fr = 0.2$, in which case the PPG dipole moves too fast (figure 7). On the other hand, the PPG model sheds too strong a wake behind the dipole, associated with a sink of energy from vortical to wave modes, and does not reproduce the vertical structure of the adjusted dipole in the form of a quasi-stationary oscillation at the front of the jet exit region. In order to obtain the latter, it is necessary to include the vortical–wave–wave interactions of P2G (figure 8), which transfer energy from wave modes to vortical modes and allow for the formation of a more realistic adjusted dipole/jet structure.

To further investigate the direction of energy transfer from vortical to wave modes and vice versa, we studied Boussinesq decay from random initial conditions. Two 'extreme' cases are illustrative: random initial conditions projecting onto (i) the vortical modes only, and (ii) the wave modes only. For $Ro = Fr = 0.2$ and random initial conditions projecting onto the vortical modes only, the PPG model acts mainly as a sink of energy from vortical to wave modes, and no coherent structures are formed (figures 10 and 13). For random initial conditions projecting onto the wave

https://doi.org/10.1017/jfm.2014.138 Published online by Cambridge University Press

modes only, PPG necessarily remains unbalanced for all times and the wave modes satisfy linear dynamics. Note that the failure of PPG for structure formation in 3D rotating Boussinesq dynamics is a stark contrast to its success for generating anticyclones in simulations of rotating shallow-water decay (RS09). For some insight into this difference between the rotating shallow-water and 3D Boussinesq systems, one may consider exact resonances of the interaction type $(0 \pm \pm)$. Exact resonances satisfy the equations $\boldsymbol{k} + \boldsymbol{p} + \boldsymbol{q} = 0$ and $\sigma^{s_k}(\boldsymbol{k}) + \sigma^{s_p}(\boldsymbol{p}) + \sigma^{s_q}(\boldsymbol{q}) = 0$, where $\sigma^{s_k}(\boldsymbol{k})$ is given by the dispersion relation for the rotating shallow-water or the 3D rotating Boussinesq equations. For $(0 \pm \pm)$ exact resonances and using the dispersion relation for rotating shallow-water flow, one finds that the vortical mode acts as a catalyst for energy transfer only between wave modes with the same wavenumber, i.e. on a wavenumber shell. In 3D Boussinesq flow on the other hand, the vortical mode acts as a catalyst for transfer of energy between wave modes which can have different wavenumbers, and hence these interactions transfer energy between scales (Lelong & Riley 1991; Bartello 1995). Thus one might expect that interactions of type $(0 \pm \pm)$ in general would be more important for 3D Boussinesq flows than for shallow-water flows. Here we have demonstrated that the $(0 \pm \pm)$ interactions are essential for the generation of hybrid vortex–gravity structures, which are not expected to form in shallow-water flows (McIntyre 2009). Some non-resonant $(0 \pm \pm)$ interactions are clearly not catalytic since they transfer energy to the vortical modes (figures 13 and 21).

As quantified by the centroid and the vorticity probability density function, the P2G model accurately captures the formation of vortices in Boussinesq decay for $Ro = Fr = 0.2$ (figures 11 and 12). For completeness, it was demonstrated that the P2G model generates cyclonic vortical columns for $Ro = 0.1$, $Fr = 1$ (figures 14 and 17), and flattened 'pancake' vortices for $Ro = 1$, $Fr = 0.1$ (figure 18), in both cases similar to the full Boussinesq system. In all parameter regimes, the presence of both $(00\pm)$ and $(0 \pm \pm)$ interactions is necessary to achieve the correct balanced end state. Furthermore, $(0 \pm \pm)$ interactions are responsible for the positive vorticity skewness of the rotation-dominated flow.

Taken together, the results show that the class of interactions involving one vortical mode and two wave modes is essential for structure formation in Boussinesq flows. This is different from the situation in shallow-water flows (McIntyre & Norton 2000; McIntyre 2009; RS09). Though FL models include the same classes of interactions contained in P2G, FL models are limited by one-way feedback as contrasted with the two-way feedback of P2G. For the long-time interaction of waves and balanced structures, the P2G model can thus extend the good agreement of an FL model (Snyder *et al.* 2009) to much longer times. Based on previous theory and simulations (Smith & Waleffe 1999, 2002; Laval *et al.* 2003; Smith & Lee 2005; Waite & Bartello 2006; Remmel *et al.* 2013), it is expected that agreement between P2G and FB will not be as close under the action of a random force at intermediate scales, at least for rotation-dominated and stratification-dominated flows, in which case there can be continual excitation of three-wave near resonances.

Acknowledgements

The authors are grateful to Dr M. Remmel for many helpful discussions and suggestions. Dr J. Tribbia and Dr R. Klein also provided valuable feedback during

https://doi.org/10.1017/jfm.2014.138 Published online by Cambridge University Press

the February 2013 Oberwolfach Workshop Geophysical Fluid Dynamics. Support for G.H.-D., L.M.S. and S.N.S. was provided by the NSF program Collaborations in Mathematical Geosciences under contract NSF-CMG-1025188.

Appendix A. Vortical–wave decomposition

The description of the intermediate models in § 3 relies on a decomposition of the vector solution into its vortical and wave components, and details of the decomposition appear in Remmel *et al.* (2010). For completeness, we include a summary here. Furthermore, we express such a decomposition with projector operators. The vortical projector acts as the identity on balanced vector solutions, and otherwise projects onto the vortical modes $\sum_{\boldsymbol{k}} b^0(\boldsymbol{k},t)\phi^0(\boldsymbol{k})\exp(\mathrm{i}\boldsymbol{k}\cdot\boldsymbol{x})$. The wave projector on the other hand projects on $\sum_{\boldsymbol{k}}\sum_{s_{\boldsymbol{k}}=\pm} b^{s_{\boldsymbol{k}}}(\boldsymbol{k},t)\phi^{s_{\boldsymbol{k}}}(\boldsymbol{k})\exp(\mathrm{i}\boldsymbol{k}\cdot\boldsymbol{x}-\sigma^{s_{\boldsymbol{k}}}(\boldsymbol{k},t)t)$. In this appendix, we explain the vortical–wave decomposition in more detail. We also present an alternative formulation of the models.

The horizontal velocity $\boldsymbol{u}_h=(u,v)$ can be written as

$$u=\chi_x-\psi_y+\overline{u(z)},\quad v=\chi_y+\psi_x+\overline{v(z)}, \tag{A 1a,b}$$

where $\overline{(\cdot)}$ denotes the horizontal average, χ corresponds to the velocity potential and ψ is the streamfunction. These relations imply

$$\nabla_h^2\chi=u_x+v_y,\quad \nabla_h^2\psi=v_x-u_y. \tag{A 2a,b}$$

For each wavevector $\boldsymbol{k}$ and each type $s_{\boldsymbol{k}}=0,\pm$, let us define the coefficient

$$a^{s_{\boldsymbol{k}}}(\boldsymbol{k},t)=b^{s_{\boldsymbol{k}}}(\boldsymbol{k},t)\exp(-\mathrm{i}\sigma^{s_{\boldsymbol{k}}}t), \tag{A 3}$$

such that

$$\begin{pmatrix}\boldsymbol{u}\\ \theta\end{pmatrix}(\boldsymbol{x},t)=\sum_{\boldsymbol{k}}\sum_{s_{\boldsymbol{k}}=0,\pm} a^{s_{\boldsymbol{k}}}(\boldsymbol{k},t)\boldsymbol{\phi}^{s_{\boldsymbol{k}}}(\boldsymbol{k})\exp(\mathrm{i}\boldsymbol{k}\cdot\boldsymbol{x})\,. \tag{A 4}$$

Using the orthonormality of eigenfunctions, we obtain

$$a_{\boldsymbol{k}}^0=\frac{\mathrm{i}N}{\sigma_{\boldsymbol{k}}k}\left(-k_h^2\psi_{\boldsymbol{k}}-\mathrm{i}\frac{f}{N}k_z\theta_{\boldsymbol{k}}\right), \tag{A 5}$$

$$a_{\boldsymbol{k}}^+=\begin{cases}\dfrac{1}{\sqrt{2}\sigma_{\boldsymbol{k}}k}\left(-\dfrac{\sigma_{\boldsymbol{k}}w_{\boldsymbol{k}}k^2}{k_h}-f\,k_zk_h\psi_{\boldsymbol{k}}+\mathrm{i}Nk_h\theta_{\boldsymbol{k}}\right) & \text{if } k_h\neq 0\\ \dfrac{1-\mathrm{i}}{2}\bar{u}+\dfrac{1+\mathrm{i}}{2}\bar{v} & \text{if } k_h=0\end{cases} \tag{A 6}$$

and

$$a_{\boldsymbol{k}}^-=\begin{cases}\dfrac{1}{\sqrt{2}\sigma_{\boldsymbol{k}}k}\left(-\dfrac{\sigma_{\boldsymbol{k}}w_{\boldsymbol{k}}k^2}{k_h}+fk_zk_h\psi_{\boldsymbol{k}}-\mathrm{i}Nk_h\theta_{\boldsymbol{k}}\right) & \text{if } k_h\neq 0\\ \dfrac{1+\mathrm{i}}{2}\bar{u}+\dfrac{1-\mathrm{i}}{2}\bar{v} & \text{if } k_h=0,\end{cases} \tag{A 7}$$

where $\sigma_{\boldsymbol{k}}=|\sigma^{\pm}(\boldsymbol{k})|$, and $\psi_{\boldsymbol{k}},\theta_{\boldsymbol{k}},w_{\boldsymbol{k}}$ are the Fourier coefficients associated with ψ,θ,w at each wavevector $\boldsymbol{k}$.

https://doi.org/10.1017/jfm.2014.138 Published online by Cambridge University Press

Notice that by adding and subtracting $a_{\boldsymbol{k}}^{+}$ and $a_{\boldsymbol{k}}^{-}$, the physical variables decouple further:

$$\left.\begin{aligned} a_{\boldsymbol{k}}^{+} + a_{\boldsymbol{k}}^{-} &= -\frac{\sqrt{2}kw_{\boldsymbol{k}}}{k_h} && (k_h \neq 0),\\ a_{k_z}^{+} + a_{k_z}^{-} &= \bar{u} + \bar{v} && (k_h = 0),\\ a_{\boldsymbol{k}}^{+} - a_{\boldsymbol{k}}^{-} &= \frac{\sqrt{2}\mathrm{i}fk_h}{\sigma_{\boldsymbol{k}}k}\left(\frac{N}{f}\theta_{\boldsymbol{k}} + \mathrm{i}k_z\psi_{\boldsymbol{k}}\right) && (k_h \neq 0),\\ a_{k_z}^{+} - a_{k_z}^{-} &= -\mathrm{i}(\bar{u} - \bar{v}) && (k_h = 0). \end{aligned}\right\} \tag{A 8}$$

Let us define

$$M = \nabla_h^2\psi - \frac{f}{N}\frac{\partial\theta}{\partial z} \quad \text{and} \quad R = \theta + \frac{f}{N}\frac{\partial\psi}{\partial z}. \tag{A 9a,b}$$

Then

$$a_{\boldsymbol{k}}^{0} = \frac{\mathrm{i}N}{\sigma_{\boldsymbol{k}}k}M_{\boldsymbol{k}}, \quad a_{\boldsymbol{k}}^{+} - a_{\boldsymbol{k}}^{-} = \frac{\sqrt{2}\mathrm{i}Nk_h}{\sigma_{\boldsymbol{k}}k}R_{\boldsymbol{k}}, \quad a_{\boldsymbol{k}}^{+} + a_{\boldsymbol{k}}^{-} = -\frac{\sqrt{2}kw_{\boldsymbol{k}}}{k_h}, \tag{A 10a,b,c}$$

when $k_h \neq 0$, where $M_{\boldsymbol{k}}$ and $R_{\boldsymbol{k}}$ are the Fourier coefficients associated with the wavevector $\boldsymbol{k}$.

The quantities M and R have physical significance: M is the linear PV and R is a measure of geostrophic imbalance. Equation (A 10) indicates that the vortical modes are all contained in the linear PV, and that the imbalance R and vertical velocity w are associated with the inertia–gravity modes. As a result, it would be more natural to write the intermediate models in terms of these variables, as they only carry out one class of modes. However, we can also present them in the standard variables $(\boldsymbol{u}, \theta)$, as it was done in (3.9).

The vortical and wave components in (3.3) can be written in terms of M, R, w, $\bar{u}(z)$ and $\bar{v}(z)$. The vortical component depends only on M, and it is given by

$$u^0 = -A_y, \quad v^0 = A_x, \quad w^0 = 0, \quad \theta^0 = -\frac{f}{N}A_z, \tag{A 11a,b,c,d}$$

where $A := \Upsilon^{-1}M$, $\Upsilon := \nabla_h^2 + ((f^2)/(N^2))\partial_{zz}$. The wave component can be written in terms of R, w, $\bar{u}(z)$ and $\bar{v}(z)$ by

$$u^{\pm} = \chi_x - \frac{f}{N}S_{yz} + \overline{u(z)}, \quad v^{\pm} = \chi_y + \frac{f}{N}S_{xz} + \overline{v(z)}, \tag{A 12a,b}$$

$$w^{\pm} = w, \quad \theta^{\pm} = \nabla_h^2 S, \tag{A 12c,d}$$

where $S := \Upsilon^{-1}R$. This yields the vortical–wave decomposition of the vector solution

$$\begin{pmatrix}\boldsymbol{u}\\ \theta\end{pmatrix} = \begin{pmatrix}\boldsymbol{u}\\ \theta\end{pmatrix}^{0} + \begin{pmatrix}\boldsymbol{u}\\ \theta\end{pmatrix}^{\pm}, \tag{A 13}$$

https://doi.org/10.1017/jfm.2014.138 Published online by Cambridge University Press

where

$$\begin{pmatrix} \boldsymbol{u} \\ \theta \end{pmatrix}^0 = \begin{pmatrix} -\partial_y \\ \partial_x \\ 0 \\ -\dfrac{f}{N}\partial_z \end{pmatrix} \left(\nabla_h^2 + \frac{f^2}{N^2}\partial_z^2\right)^{-1} \left(\partial_x v - \partial_y u - \frac{f}{N}\partial_z \theta\right). \tag{A 14}$$

On the other hand, the Boussinesq equations can be formulated in the variables M, R, w, $\bar{u}(z)$ and $\bar{v}(z)$ as

$$\left.\begin{aligned} \frac{\partial M}{\partial t} + \hat{\boldsymbol{z}} \cdot \boldsymbol{\nabla} \times (\boldsymbol{u} \cdot \boldsymbol{\nabla}\boldsymbol{u}) - \frac{f}{N}\partial_z \left[\boldsymbol{u} \cdot \boldsymbol{\nabla}\theta\right] &= 0, \\ \frac{\partial \nabla_h^2 R}{\partial t} - N\Upsilon w + \nabla_h^2 \left[\boldsymbol{u} \cdot \boldsymbol{\nabla}\theta\right] + \frac{f}{N}\partial_z(\hat{\boldsymbol{z}} \cdot \boldsymbol{\nabla} \times (\boldsymbol{u} \cdot \boldsymbol{\nabla}\boldsymbol{u})) &= 0, \\ \frac{\partial \nabla^2 w}{\partial t} + N\nabla_h^2 R + \nabla_h^2(\boldsymbol{u} \cdot \boldsymbol{\nabla} w) - \partial_z(\boldsymbol{\nabla}_h \cdot (\boldsymbol{u} \cdot \boldsymbol{\nabla}\boldsymbol{u}_h)) &= 0, \\ \frac{\partial \overline{u(z)}}{\partial t} - f\overline{v(z)} + \overline{\partial_z(uw)} &= 0, \\ \frac{\partial \overline{v(z)}}{\partial t} + f\overline{u(z)} + \overline{\partial_z(vw)} &= 0. \end{aligned}\right\} \tag{A 15}$$

We note that the system above is closed. Given M, R, w, $\bar{u}(z)$ and $\bar{v}(z)$, $\boldsymbol{u}$ and θ can be recovered by (A 1) and the relations

$$\psi = A + \frac{f}{N}S_z, \quad \theta = \nabla_h^2 S - \frac{f}{N}A_z, \quad \nabla_h^2 \chi = -w_z. \tag{A 16}$$

The intermediate models studied here and first introduced in Remmel *et al.* (2010) result from restricting the interaction coefficients in (2.8) to certain classes of interactions. This can be easily done in physical space using (A 15) and identifying M with vortical modes and R, w, $\bar{u}(z)$ and $\bar{v}(z)$ with inertia–gravity waves. One can then obtain the PPG model in these variables, which is given by

$$\left.\begin{aligned} &\frac{\partial M}{\partial t} + \hat{\boldsymbol{z}} \cdot \boldsymbol{\nabla} \times (\boldsymbol{u}^0 \cdot \boldsymbol{\nabla}\boldsymbol{u}^0) + \hat{\boldsymbol{z}} \cdot \boldsymbol{\nabla} \times (\boldsymbol{u}^0 \cdot \boldsymbol{\nabla}\boldsymbol{u}^\pm) + \hat{\boldsymbol{z}} \cdot \boldsymbol{\nabla} \times (\boldsymbol{u}^\pm \cdot \boldsymbol{\nabla}\boldsymbol{u}^0) \\ &\qquad - \frac{f}{N}\partial_z \left[\boldsymbol{u}^0 \cdot \boldsymbol{\nabla}\theta^0\right] - \frac{f}{N}\partial_z \left[\boldsymbol{u}^\pm \cdot \boldsymbol{\nabla}\theta^0\right] - \frac{f}{N}\partial_z \left[\boldsymbol{u}^0 \cdot \boldsymbol{\nabla}\theta^\pm\right] = 0, \\ &\frac{\partial \nabla_h^2 R}{\partial t} - N\Upsilon w + \nabla_h^2 \left[\boldsymbol{u}^0 \cdot \boldsymbol{\nabla}\theta^0\right] + \frac{f}{N}\partial_z(\hat{\boldsymbol{z}} \cdot \boldsymbol{\nabla} \times (\boldsymbol{u}^0 \cdot \boldsymbol{\nabla}\boldsymbol{u}^0)) = 0, \\ &\frac{\partial \nabla^2 w}{\partial t} + N\nabla_h^2 R - \partial_z(\boldsymbol{\nabla}_h \cdot (\boldsymbol{u}^0 \cdot \boldsymbol{\nabla}\boldsymbol{u}_h^0)) = 0, \\ &\frac{\partial \overline{u(z)}}{\partial t} - f\overline{v(z)} = 0, \\ &\frac{\partial \overline{v(z)}}{\partial t} + f\overline{u(z)} = 0. \end{aligned}\right\} \tag{A 17}$$

We refer the reader to Remmel (2010) for a detailed description of the other intermediate models using the approach above, which are included in the next appendix for completeness. The equivalent models for the shallow-water equations and their properties can be found in RS09.

https://doi.org/10.1017/jfm.2014.138 Published online by Cambridge University Press

Appendix B. Derivation of the P2SG, P2G and QG models

The intermediate models studied in this paper were explained in § 3. The nonlinear interactions included in each model are summarized in table 1. Only details about PPG were provided. For the sake of completeness, in this appendix we describe the rest of the models in the form described in § 3, and in the form considered in appendix A. See Remmel (2010) for more details.

The P2SG model includes the following interactions: vortical–vortical–vortical and vortical–wave–wave. The model in physical space can be written as

$$\left.\begin{aligned} &\frac{\partial}{\partial t}\begin{pmatrix}\boldsymbol{u}\\ \theta\end{pmatrix}+\begin{pmatrix}\boldsymbol{u}^0\cdot\boldsymbol{\nabla}\boldsymbol{u}^0+\boldsymbol{u}^\pm\cdot\boldsymbol{\nabla}\boldsymbol{u}^\pm\\ \boldsymbol{u}^0\cdot\boldsymbol{\nabla}\theta^0+\boldsymbol{u}^\pm\cdot\boldsymbol{\nabla}\theta^\pm\end{pmatrix}^0+\begin{pmatrix}\boldsymbol{u}^0\cdot\boldsymbol{\nabla}\boldsymbol{u}^\pm+\boldsymbol{u}^\pm\cdot\boldsymbol{\nabla}\boldsymbol{u}^0\\ \boldsymbol{u}^0\cdot\boldsymbol{\nabla}\theta^\pm+\boldsymbol{u}^\pm\cdot\boldsymbol{\nabla}\theta^0\end{pmatrix}^\pm\\ &\qquad+\begin{pmatrix}f\hat{\boldsymbol{z}}\times\boldsymbol{u}+N\theta\hat{\boldsymbol{z}}\\ -N\boldsymbol{u}\cdot\hat{\boldsymbol{z}}\end{pmatrix}=\begin{pmatrix}-\boldsymbol{\nabla}p\\ 0\end{pmatrix},\\ &\boldsymbol{\nabla}\cdot\boldsymbol{u}=0.\end{aligned}\right\}\tag{B 1}$$

In the $M, R, w, \bar{u}(z)$ and $\bar{v}(z)$ variables, it can be written as

$$\left.\begin{aligned} &\frac{\partial M}{\partial t}+\hat{\boldsymbol{z}}\cdot\boldsymbol{\nabla}\times(\boldsymbol{u}^0\cdot\boldsymbol{\nabla}\boldsymbol{u}^0)+\hat{\boldsymbol{z}}\cdot\boldsymbol{\nabla}\times(\boldsymbol{u}^\pm\cdot\boldsymbol{\nabla}\boldsymbol{u}^\pm)\\ &\qquad-\frac{f}{N}\partial_z\left[\boldsymbol{u}^0\cdot\boldsymbol{\nabla}\theta^0\right]-\frac{f}{N}\partial_z\left[\boldsymbol{u}^\pm\cdot\boldsymbol{\nabla}\theta^\pm\right]=0,\\ &\frac{\partial\nabla_h^2R}{\partial t}-N\Upsilon w+\nabla_h^2\left[\boldsymbol{u}^0\cdot\boldsymbol{\nabla}\theta^\pm\right]+\nabla_h^2\left[\boldsymbol{u}^\pm\cdot\boldsymbol{\nabla}\theta^0\right]\\ &+\frac{f}{N}\partial_z(\hat{\boldsymbol{z}}\cdot\boldsymbol{\nabla}\times(\boldsymbol{u}^0\cdot\boldsymbol{\nabla}\boldsymbol{u}^\pm))+\frac{f}{N}\partial_z(\hat{\boldsymbol{z}}\cdot\boldsymbol{\nabla}\times(\boldsymbol{u}^\pm\cdot\boldsymbol{\nabla}\boldsymbol{u}^0))=0,\\ &\frac{\partial\nabla^2w}{\partial t}+N\nabla_h^2R+\nabla_h^2(\boldsymbol{u}^0\cdot\boldsymbol{\nabla}w)-\partial_z(\boldsymbol{\nabla}_h\cdot(\boldsymbol{u}^0\cdot\boldsymbol{\nabla}\boldsymbol{u}_h^\pm))\\ &\qquad-\partial_z(\boldsymbol{\nabla}_h\cdot(\boldsymbol{u}^\pm\cdot\boldsymbol{\nabla}\boldsymbol{u}_h^0))=0,\\ &\frac{\partial\overline{u(z)}}{\partial t}-f\overline{v(z)}+\overline{\partial_z(u^0w)}=0,\\ &\frac{\partial\overline{v(z)}}{\partial t}+f\overline{u(z)}+\overline{\partial_z(v^0w)}=0.\end{aligned}\right\}\tag{B 2}$$

The P2G model includes the following interactions: vortical–vortical–vortical, vortical–vortical–wave and vortical–wave–wave. The model in physical space can be written as

$$\left.\begin{aligned} &\frac{\partial}{\partial t}\begin{pmatrix}\boldsymbol{u}\\ \theta\end{pmatrix}+\begin{pmatrix}\boldsymbol{u}\cdot\boldsymbol{\nabla}\boldsymbol{u}\\ \boldsymbol{u}\cdot\boldsymbol{\nabla}\theta\end{pmatrix}^0+\begin{pmatrix}\boldsymbol{u}^0\cdot\boldsymbol{\nabla}\boldsymbol{u}^0+\boldsymbol{u}^0\cdot\boldsymbol{\nabla}\boldsymbol{u}^\pm+\boldsymbol{u}^\pm\cdot\boldsymbol{\nabla}\boldsymbol{u}^0\\ \boldsymbol{u}^0\cdot\boldsymbol{\nabla}\theta^0+\boldsymbol{u}^0\cdot\boldsymbol{\nabla}\theta^\pm+\boldsymbol{u}^\pm\cdot\boldsymbol{\nabla}\theta^0\end{pmatrix}^\pm\\ &\qquad+\begin{pmatrix}f\hat{\boldsymbol{z}}\times\boldsymbol{u}+N\theta\hat{\boldsymbol{z}}\\ -N\boldsymbol{u}\cdot\hat{\boldsymbol{z}}\end{pmatrix}=\begin{pmatrix}-\boldsymbol{\nabla}p\\ 0\end{pmatrix},\\ &\boldsymbol{\nabla}\cdot\boldsymbol{u}=0.\end{aligned}\right\}\tag{B 3}$$

https://doi.org/10.1017/jfm.2014.138 Published online by Cambridge University Press

In the $M, R, w, \bar{u}(z)$ and $\bar{v}(z)$ variables, it can be written as

$$\left.\begin{aligned}
\frac{\partial M}{\partial t} + \hat{\boldsymbol{z}}\cdot\boldsymbol{\nabla}\times(\boldsymbol{u}\cdot\boldsymbol{\nabla}\boldsymbol{u}) - \frac{f}{N}\partial_z\left[\boldsymbol{u}\cdot\boldsymbol{\nabla}\theta\right] &= 0,\\
\frac{\partial \nabla_h^2 R}{\partial t} - N\Upsilon w + \nabla_h^2\left[\boldsymbol{u}^0\cdot\boldsymbol{\nabla}\theta^0\right] + \nabla_h^2\left[\boldsymbol{u}^0\cdot\boldsymbol{\nabla}\theta^{\pm}\right] + \nabla_h^2\left[\boldsymbol{u}^{\pm}\cdot\boldsymbol{\nabla}\theta^0\right]&\\
+\frac{f}{N}\partial_z(\hat{\boldsymbol{z}}\cdot\boldsymbol{\nabla}\times(\boldsymbol{u}^0\cdot\boldsymbol{\nabla}\boldsymbol{u}^0)) + \frac{f}{N}\partial_z(\hat{\boldsymbol{z}}\cdot\boldsymbol{\nabla}\times(\boldsymbol{u}^0\cdot\boldsymbol{\nabla}\boldsymbol{u}^{\pm}))&\\
+\frac{f}{N}\partial_z(\hat{\boldsymbol{z}}\cdot\boldsymbol{\nabla}\times(\boldsymbol{u}^{\pm}\cdot\boldsymbol{\nabla}\boldsymbol{u}^0)) &= 0,\\
\frac{\partial \nabla^2 w}{\partial t} + N\nabla_h^2 R + \nabla_h^2(\boldsymbol{u}^0\cdot\boldsymbol{\nabla}w) - \partial_z(\boldsymbol{\nabla}_h\cdot(\boldsymbol{u}^0\cdot\boldsymbol{\nabla}\boldsymbol{u}_h^0))&\\
-\partial_z(\boldsymbol{\nabla}_h\cdot(\boldsymbol{u}^0\cdot\boldsymbol{\nabla}\boldsymbol{u}_h^{\pm})) - \partial_z(\boldsymbol{\nabla}_h\cdot(\boldsymbol{u}^{\pm}\cdot\boldsymbol{\nabla}\boldsymbol{u}_h^0)) &= 0\\
\frac{\partial\overline{u(z)}}{\partial t} - f\overline{v(z)} + \overline{\partial_z(u^0w)} &= 0,\\
\frac{\partial\overline{v(z)}}{\partial t} + f\overline{u(z)} + \overline{\partial_z(v^0w)} &= 0.
\end{aligned}\right\} \tag{B 4}$$

The QG model fits at the bottom of the hierarchy of the models considered here, and it only contains vortical–vortical–vortical interactions. The model in physical space can be written as

$$\left.\begin{aligned}
&\frac{\partial}{\partial t}\begin{pmatrix}\boldsymbol{u}\\ \theta\end{pmatrix} + \begin{pmatrix}\boldsymbol{u^0}\cdot\boldsymbol{\nabla}\boldsymbol{u^0}\\ \boldsymbol{u^0}\cdot\boldsymbol{\nabla}\theta^0\end{pmatrix}^0 = \boldsymbol{0},\\
&\boldsymbol{\nabla}\cdot\boldsymbol{u} = 0.
\end{aligned}\right\} \tag{B 5}$$

which can easily be transformed to the standard QG equations assuming the solution is initially balanced:

$$\frac{\partial M}{\partial t} + J(\psi, M) = 0, \quad M = \left(\nabla_h^2 + \frac{f^2}{N^2}\partial_z\right)\psi, \tag{B 6a,b}$$

where $J(A, B) = A_xB_y - A_yB_x$ is the Jacobian, M is the linear PV and ψ is the streamfunction, so that $u = -\partial_y\psi$, $v = \partial_x\psi$, $w = 0$, $\theta = -(f/N)\partial_z\psi$.

REFERENCES

ALLEN, J. S. 1993 Iterated geostrophic intermediate models. *J. Phys. Oceanogr.* **23**, 2447–2461.

BABIN, A., MAHALOV, A. & NICOLAENKO, B. 2000 Global regularity of 3D rotating Navier–Stokes equations for resonant domains. *Appl. Maths Comput.* **13** (4), 51–57.

BARTELLO, P. 1995 Geostrophic adjustment and inverse cascades in rotating stratified turbulence. *J. Atmos. Sci.* **52**, 4410–4428.

BOUROUIBA, L. & BARTELLO, P. 2007 The intermediate Rossby number range and two-dimensional–three-dimensional transfers in rotating decaying homogeneous turbulence. *J. Fluid Mech.* **597**, 139–161.

BOYD, J. P. 2001 *Chebyshev and Fourier Special Methods*. Dover.

CAILLOL, P. & ZEITLIN, V. 2000 Kinetic equations and stationary energy spectra of weakly nonlinear internal gravity waves. *Dyn. Atmos. Oceans* **32** (2), 81–112.

CAMBON, C., MANSOUR, N. N. & GODEFERD, F. S. 1997 Energy transfer in rotating turbulence. *J. Fluid Mech.* **337**, 303–332.

https://doi.org/10.1017/jfm.2014.138 Published online by Cambridge University Press

CAMBON, C., RUBINSTEIN, R. & GODEFERD, F. S. 2004 Advances in wave turbulence: rapidly rotating flows. *New J. Phys.* **6** (1), 73.

CANUTO, C., HUSSAINI, M. Y., QUARTERONI, A. & ZHANG, T. A. 2006 *Spectral Methods: Fundamentals in Single Domains*. Springer.

CHARNEY, J. G. 1948 On the scale of atmospheric motions. *Geofys. Publ. Norske Vid.-Akad. Oslo* **17** (2), 251–261.

CUNNINGHAM, P. & KEYSER, D. 2004 Dynamics of jet streaks in a stratified quasi-geostrophic atmosphere: steady-state representations. *Q. J. R. Meteorol. Soc.* **130** (600), 1579–1609.

DEUSEBIO, E., VALLGREN, A. & LINDBORG, E. 2013 The route to dissipation in strongly stratified and rotating flows. *J. Fluid Mech.* **720**, 66–103.

EMBID, P. F. & MAJDA, A. J. 1998 Low Froude number limiting dynamics for stably stratified flow with small or finite Rossby numbers. *Geophys. Astrophys. Fluid Dyn.* **87** (1–2), 1–50.

FLIERL, G. R. 1987 Isolated eddy models in geophysics. *Annu. Rev. Fluid Mech.* **19**, 493–530.

FORD, R., MCINTYRE, M. E. & NORTON, W. A. 2000 Balance and the slow quasi manifold: some explicit results. *J. Atmos. Sci.* **57**, 1236–1254.

FRITTS, D. C. & ALEXANDER, M. J. 2003 Gravity wave dynamics and effects in the middle atmosphere. *Rev. Geophys.* **41** (1), 1003.

GALTIER, S. 2003 Weak inertial-wave turbulence theory. *Phys. Rev.* E **68** (1), 015301.

GILL, A. E. 1982 *Atmosphere-Ocean Dynamics*. Academic.

GREENSPAN, H. P. 1968 *The Theory of Rotating Fluids*. Cambridge University Press.

HAKIM, G. J., SNYDER, C. & MURAKI, D. J. 2002 A new surface model for cyclone-anticyclone asymmetry. *J. Atmos. Sci.* **59**, 2405–2420.

HASSELMANN, K. 1962 On the nonlinear energy transfer in a gravity-wave spectrum. Part 1. General theory. *J. Fluid Mech.* **12** (4), 481–500.

HOPFINGER, E. J., BROWAND, F. K. & GAGNE, Y. 1982 Turbulence and waves in a rotating tank. *J. Fluid Mech.* **125**, 505–534.

KIZNER, Z., REZNIK, G., FRIDMAN, B., KHVOLES, R. & MCWILLIAMS, J. 2008 Shallow water modons on the f-plane. *J. Fluid Mech.* **603**, 305–329.

KRAICHNAN, R. H. 1973 Helical turbulence and absolute equilibrium. *J. Fluid Mech.* **59**, 745–752.

KUO, A. C. & POLVANI, L. M. 2000 Nonlinear geostrophic adjustment, cyclone/anticyclone asymmetry, and potential vorticity rearrangement. *Phys. Fluids* **12** (5), 1087–1100.

LAVAL, J. P., MCWILLIAMS, J. C. & DUBRULLE, B. 2003 Forced stratified turbulence: successive transitions with Reynolds number. *Phys. Rev.* E **68**, 36308.

LEDWELL, J. R., MONTGOMERY, E. T., POLZIN, K. L., LAURENT, L. C. ST., SCHMITT, R. W. & TOOLE, J. M. 2000 Evidence for enhanced mixing over rough topography in the abyssal ocean. *Nature* **403** (6766), 179–182.

LEE, Y. & SMITH, L. M. 2007 On the formation of geophysical and planetary zonal flows by near-resonant wave interactions. *J. Fluid Mech.* **576**, 405–424.

LELONG, M.-P. & RILEY, J. J. 1991 Internal wave–vortical mode interactions in strongly stratified flows. *J. Fluid Mech.* **232**, 1–19.

LORENZ, E. N. & KRISHNAMURTHY, V. 1987 On the nonexistence of a slow manifold. *J. Atmos. Sci.* **44**, 2940–2950.

LVOV, Y. V., POLZIN, K. L. & TABAK, E. G. 2004 Energy spectra of the ocean's internal wavefield: theory and observations. *Phys. Rev. Lett.* **92** (12), 128501.

LVOV, Y. V., POLZIN, K. L. & YOKOYAMA, N. 2012 Resonant and near-resonant internal wave interactions. *J. Phys. Oceanogr.* **42** (5), 669–691.

MAJDA, A. 2003 *Introduction to PDEs and Waves for the Atmosphere and Ocean.. (Courant Lecture Notes in Mathematics)*, vol. 9. New York University Courant Institute of Mathematical Sciences.

MCCOMAS, C. H. & BRETHERTON, F. P. 1977 Resonant interaction of oceanic internal waves. *J. Geophys. Res.* **82** (9), 1397–1412.

MCINTYRE, M. E. 2009 Spontaneous imbalance and hybrid vortex-gravity structures. *J. Atmos. Sci.* **66** (5), 1315–1326.

MCINTYRE, M. E. & NORTON, W. A. 2000 Potential vorticity inversion on a hemisphere. *J. Atmos. Sci.* **57** (9), 1214–1235.

https://doi.org/10.1017/jfm.2014.138 Published online by Cambridge University Press

McWilliams, J. C. & Gent, P. R. 1980 Intermediate models of planetary circulations in the atmosphere and ocean. *J. Atmos. Sci.* **37**, 1657–1678.

Metais, O., Bartello, P., Garnier, E., Riley, J. J. & Lesieur, M. 1996 Inverse cascade in stably stratified rotating turbulence. *Dyn. Atmos. Oceans* **23** (1), 193–203.

Mohebalhojeh, A. R. & Dritschel, D. G. 2001 Hierarchies of balance conditions for the f-plane shallow-water equations. *J. Atmos. Sci.* **58** (16), 2411–2426.

Muraki, D. J. & Hakim, G. J. 2001 Balanced asymmetries of waves on the tropopause. *J. Atmos. Sci.* **58** (3), 237–252.

Muraki, D. J., Snyder, C. & Rotunno, R. 1999 The next-order corrections to quasigeostrophic theory. *J. Atmos. Sci.* **56** (11), 1547–1560.

Newell, A. C. 1969 Rossby wavepacket interactions. *J. Fluid Mech.* **35** (2), 255–271.

O'Sullivan, D. & Dunkerton, T. J. 1995 Generation of inertia-gravity waves in a simulated life cycle of baroclinic instability. *J. Atmos. Sci.* **52**, 3695–3716.

Pedlosky, J. 1982 *Geophysical Fluid Dynamics*. Springer.

Plougonven, R. & Zeitlin, V. 2002 Internal gravity wave emission from a pancake vortex: an example of wave–vortex interaction in strongly stratified flows. *Phys. Fluids* **14** (3), 1259–1268.

Polvani, L. M., McWilliams, J. C., Spall, M. A. & Ford, R. 1994 The coherent structures of shallow-water turbulence: deformation-radius effects, cyclone/anticyclone asymmetry and gravity-wave generation. *Chaos* **4** (2), 177–186.

Praud, O., Sommeria, J. & Fincham, A. M. 2007 Decaying grid turbulence in a rotating stratified fluid. *J. Fluid Mech.* **547**, 389–412.

Remmel, M. 2010 New models for the rotating shallow water and Boussinesq equations by subsets of mode interactions. ProQuest LLC, Ann Arbor, MI; PhD thesis, The University of Wisconsin–Madison.

Remmel, M. & Smith, L. M. 2009 New intermediate models for rotating shallow water and an investigation of the preference for anticyclones. *J. Fluid Mech.* **635**, 321–359.

Remmel, M., Sukhatme, J. & Smith, L. M. 2010 Nonlinear inertia-gravity wave-mode interactions in three dimensional rotating stratified flows. *Commun. Math. Sci.* **8** (2), 357–376.

Remmel, M., Sukhatme, J. & Smith, L. 2014 Nonlinear gravity-wave interactions in stratified turbulence. *Theor. Comp. Fluid. Dyn.* **28** (2), 131–145.

Ribstein, B., Gula, J. & Zeitlin, V. 2010 (A)geostrophic adjustment of dipolar perturbations, formation of coherent structures and their properties, as follows from high-resolution numerical simulations with rotating shallow water model. *Phys. Fluids* **22**, 116603.

Salmon, R. 1998 *Lectures on Geophysical Fluid Dynamics*. Oxford University Press.

Smith, L. M. & Lee, Y. 2005 On near resonances and symmetry breaking in forced rotating flows at moderate Rossby number. *J. Fluid Mech.* **535**, 111–142.

Smith, L. M. & Waleffe, F. 1999 Transfer of energy to two-dimensional large scales in forced, rotating three-dimensional turbulence. *Phys. Fluids* **11** (6), 1608–1622.

Smith, L. M. & Waleffe, F. 2002 Generation of slow large scales in forced rotating stratified turbulence. *J. Fluid Mech.* **451**, 145–168.

Snyder, C. 1999 Error growth in flows with finite-amplitude waves or coherent structures. *J. Atmos. Sci.* **56**, 500–506.

Snyder, C., Muraki, D. J., Plougonven, R. & Zhang, F. 2007 Inertia-gravity waves generated within a dipole vortex. *J. Atmos. Sci.* **64** (12), 4417–4431.

Snyder, C., Plougonven, R. & Muraki, D. J. 2009 Mechanisms for spontaneous gravity wave generation within a dipole vortex. *J. Atmos. Sci.* **66** (11), 3464–3478.

Spiegel, E. A. & Veronis, G. 1960 On the Boussinesq approximation for a compressible fluid. *Astrophys. J.* **131**, 442–447.

Vallis, G. K. 1996 Potential vorticity inversion and balanced equations of motion for rotating and stratified flows. *Q. J. R. Meteorol. Soc.* **122** (529), 291–322.

Vallis, G. K. 2006 *Atmospheric and Oceanic Fluid Dynamics: Fundamentals and Large-Scale Circulation*. Cambridge University Press.

https://doi.org/10.1017/jfm.2014.138 Published online by Cambridge University Press

VANNESTE, J. 2013 Balance and spontaneous wave generation in geophysical flows. *Annu. Rev. Fluid Mech.* **45**, 147–172.

VANNESTE, J. & YAVNEH, I. 2004 Exponentially small inertia-gravity waves and the breakdown of quasigeostrophic balance. *J. Atmos. Sci.* **61**, 211–223.

VIÚDEZ, Á. 2007 The origin of the stationary frontal wavepacket spontaneously generated in rotating stratified vortex dipoles. *J. Fluid Mech.* **593**, 359–383.

WAITE, M. L. & BARTELLO, P. 2006 The transition from geostrophic to stratified turbulence. *J. Fluid Mech.* **568**, 89–108.

WALEFFE, F. 1993 Inertial transfers in the helical decomposition. *Phys. Fluids* A **5**, 677–685.

WANG, S. & ZHANG, F. 2010 Source of gravity waves within a vortex-dipole jet revealed by a linear model. *J. Atmos. Sci.* **67** (5), 1438–1455.

WANG, S., ZHANG, F. & EPIFANIO, C. C. 2010 Forced gravity wave response near the jet exit region in a linear model. *Q. J. R. Meteorol. Soc.* **136**, 1773–1787.

WANG, S., ZHANG, F. & SNYDER, C. 2009 Generation and propagation of inertia-gravity waves from vortex dipoles and jets. *J. Atmos. Sci.* **66** (5), 1294–1314.

WARN, T., BOKHOVE, O., SHEPHERD, T. G. & VALLIS, G. K. 1995 Rossby number expansions, slaving principles, and balance dynamics. *Q. J. R. Meteorol. Soc.* **121** (523), 723–739.

WARNER, C. D. & MCINTYRE, M. E. 2001 An ultrasimple spectral parameterization for nonorographic gravity waves. *J. Atmos. Sci.* **58** (14), 1837–1857.

WUNSCH, C. & FERRARI, R. 2004 Vertical mixing, energy, and the general circulation of the oceans. *Annu. Rev. Fluid Mech.* **36**, 281–314.

ZAKHAROV, V. E., LVOV, V. S. & FALKOVICH, G. 1992 *Kolmogorov Spectra of Turbulence 1. Wave Turbulence*. Springer.

ZEITLIN, V. 2008 Decoupling of balanced and unbalanced motions and inertia-gravity wave emission: small versus large rossby numbers. *J. Atmos. Sci.* **65** (11), 3528–3542.

https://doi.org/10.1017/jfm.2014.138 Published online by Cambridge University Press